Mineralogy and petrology of listvenites from the Oman ophiolite: effects of fluid-rock interactions and carbonation on ultramafic rocks

E.L. Boter

MSc thesis

Supervisors: dr. Andreas Beinlich & dr. Oliver Plümper

Department of Earth Sciences, Utrecht University

Department of Applied Geology, Curtin University

Utrecht University

Curtin University

Abstract

Mineral replacement reactions during carbonation of ultramafic rocks lead to the formation of carbonate-bearing reaction product assemblages. These include ophicarbonate (assemblage of serpentine and carbonate), soapstone (consists mostly of talc) and listvenite (carbonate, quartz and fuchsite assemblage). Samples were collected from serpentinites, ophicarbonates and listvenites from the Semail ophiolite during the Oman Drilling Project (ODP), which has been exposed to extensive hydrothermal alteration. The objective of this research is to study the chemical composition and alteration textures of carbonated ultramafic rocks in order to determine the effects of fluid-rock interactions and the evolution of carbonation, with emphasis on the onset of carbonation. Optical and electron microscopy show that the mineral assemblage of ophicarbonates consists of serpentine, magnesite, dolomite, magnetite, chromite, Cr-spinel and relicts of orthopyroxene. Listvenites contain magnesite, dolomite, quartz, magnetite, hematite (in the upper listvenites) and fuchsite (in the lower listvenites). Both ophicarbonates and listvenites have been subjected to extensive veining, reflecting the presence of pathways for CO_2-rich fluids that led to carbonation. The timing of vein formation is determined by cross-cutting relationships; serpentine veining is followed by formation of magnesite, quartz and dolomite veins, respectively. Carbonate spherules observed in ophicarbonates and listvenites represent the initial stage of carbonation in serpentinite, and can be traced into strongly carbonated samples. The features have a magnesite core and dolomite (in ophicarbonates) or Ca-rich magnesite (in listvenites) rim. Optical and electron microscopy, X-ray micro CT scanning and Tescan Integrated Mineral Analysis (TIMA) prove that spherules first appear as separate features, mostly concentrated around carbonate veins, but evolve into aggregates and finally into euhedrally overgrown textures. The presence of compositionally varying veins and zoned carbonate spherules demonstrate that carbonation occurred under the influence of a changing fluid composition. Serpentinization of peridotites was followed by carbonation, leading to the production of magnesite veins and carbonate spherules. The breakdown of magnetite, chromite and other oxides provided Fe for zoned spherules and veins. Continued carbonation led to the formation of quartz, and Ca-rich fluids ultimately produced dolomite and Ca-rich carbonate veins and spherules.

Table of contents

1. Introduction

Understanding the carbon flux in subduction zones is essential to fully comprehend the global carbon cycle and transfer processes between the Earth's crust and mantle. However, carbon cycling in subduction zone settings remains poorly understood. Several studies have estimated that half of the subducted carbon is recycled into the convecting mantle (Gorman et al., 2006; Dasgupta and Hirschmann, 2010), but a recent study by Kelemen and Manning (2015) has implied that most of the carbon is removed from the subducting plate and transported into the mantle lithosphere and crust. It has been inferred that there is no substantial carbon transfer within subduction zones at depths above 60-70 km (Gorman et al., 2006; Dasgupta and Hirschmann, 2010), but the presence of carbonated ultramafic rocks (listvenites) in ophiolites thrust over metasediments indicates significant carbon transfer at low temperatures (Falk and Kelemen, 2015; Kelemen and Manning, 2015). Listvenites thus represent an important carbon sink in subduction settings and may provide boundary conditions for the evaluation of carbon transfer between the crust and mantle.

Listvenites are described as an assemblage composed of carbonate, quartz and fuchsite, in combination with sulphides and other accessory minerals (Rose, 1837; Halls and Zhao, 1995). The rocks are characterized by a striking green colour in hand specimen due to the presence of fuchsite, whereas surface samples appear reddish brown due to weathering and oxidation of iron bearing carbonates to iron oxides (Halls and Zhao, 1995; Emam and Zoheir, 2013). Listvenites are formed by metasomatic alteration of ultramafic rocks, such as peridotites and serpentinites, due to carbonation associated with K-bearing fluids (Halls and Zhao, 1995; Nasir et al., 2007; Falk and Kelemen, 2015).

Listvenites were initially studied because of their association with gold and other economically valuable ore deposits, but more recently have attracted attention as an option for permanent carbon storage (Kelemen and Matter, 2008; Beinlich et al., 2012; Streit et al., 2012; Falk and Kelemen, 2015). Several studies on naturally carbonated peridotites have been carried out to determine the reaction rate and extent of carbonation (Hansen et al., 2005; Kelemen and Matter, 2008; Matter and Kelemen, 2009; Paukert et al., 2012), leading to the conclusion that the reaction would be limited due to porosity and permeability clogging caused by a volume increase during peridotite carbonation and hydration. However, mantle peridotites are often serpentinized since they are not stable at the Earth's surface, and thus easily react with fluids (Streit et al., 2012). Even though the carbonation rate of serpentinite is slower than that of mantle peridotite, serpentinite may pose as a more feasible option for CO_2 sequestration due to the reduced chance of clogging (Hansen et al., 2005; Gerdemann et al., 2007; Beinlich et al., 2012). Carbonation of ultramafic rocks such as serpentinite involves the replacement of silicate minerals (e.g. serpentine and clinopyroxene) by carbonates (e.g. magnesite or dolomite), as the silicates donate bivalent cations such as Fe^{2+}, Mg^{2+} and Ca^{2+} (Halls and Zhao, 1995; Hansen et al., 2005). This reaction, which fixates CO_2 in carbonate minerals, releases water and silica, which may later precipitate as quartz:

$$(Mg,Fe)_3Si_2O_5(OH)_4 + 3\ CO_2 \rightarrow 3\ (Mg,Fe)CO_3 + 2\ SiO_2 + 2\ H_2O\ (1)$$
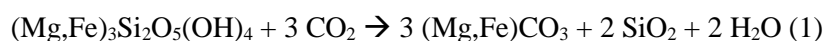
Natural CO_2 sequestration by carbonation of ultramafic rocks is an important carbon sink, and occurs in a number of different locations. Massive serpentinite carbonation at Linnajavri, Norway, has been described by Beinlich et al. (2012), who observed that a serpentinized ophiolite had been altered to soapstone and listvenite. Talc is observed as a dominant component in soapstone and forms a minor constituent of the listvenites. Assemblages of serpentine, magnesite, talc and quartz have also been observed at Atlin, Canada, by Hansen et al. (2005), who argue that alteration of peridotite occurs via a series of carbonation reactions that ultimately lead to the listvenite assemblage of quartz and magnesite. Olivine would first react with CO_2 and water to form serpentine and magnesite, after which serpentine undergoes carbonation and forms magnesite and talc. During the last step, talc would react with CO_2 to form the typical listvenite assemblage of magnesite and quartz.

Extensive serpentinization and carbonation is observed in the peridotites of the Semail ophiolite in Oman, which is the focus of this study. Listvenites mostly occur along major fault zones and are spatially related to extremely serpentinized porous and fractured peridotites (Nasir et al., 2007; Falk and Kelemen, 2015). This setting creates a network of faults and fractures that allow infiltration of CO_2-bearing fluid through high permeability pathways (Halls and Zhao, 1995; Hansen et al., 2005). There is no consensus yet on the nature of the fluids that have led to the formation of listvenites. Stanger (1985) argues that slightly acidic, CO_2-bearing groundwater infiltrated and altered serpentinites due to Paleogene faulting. More recently, it has been proposed that serpentinites have reacted with CO_2-bearing, sediment-derived fluids during obduction of the Semail ophiolite (Kelemen et al., 2011; Falk and Kelemen, 2015).

In this study, observations from fifteen samples taken from the Semail Ophiolite during the Oman Drilling Project are presented. The aim of the Oman Drilling Project is to sample the complete ophiolite sequence, from crust to upper mantle, to understand the processes that produce and alter oceanic crust and shallow mantle. These include formation of oceanic lithosphere at mid-oceanic ridges, hydrothermal alteration of oceanic crust, and transport of volatile elements in subduction zones. The samples used for this study include heavily carbonated serpentinites and listvenites, representing a high degree of hydrothermal alteration. The objective of this research is to investigate the mineralogy and petrology of these samples, and to document extensive veining and growth of carbonate in order to determine the alteration history and the effects of fluid flow through ultramafic rocks. On the basis of small-scale carbonate spherules within carbonated serpentinites and listvenites, an explanation for the initiation and evolution of carbonation is provided.

2. Geological Setting

The Semail Ophiolite, located in the Sultanate of Oman and the United Arab Emirates (Figure 1a), is the largest ophiolite sequence in the world and has been the site of many studies on the serpentinization and carbonation of oceanic crust. The samples used for this study were collected from Hole BT1B, located in the Semail Massif (Figure 1b). During the first phase of the ICDP Oman Drilling Project, BT1B was drilled to a total depth of 300 m. The core includes a sequence of listvenites alternating with serpentinites and ophicarbonates, a small section of cataclasites, and a sequence of metasediments and metabasalts, which make up the metamorphic sole.
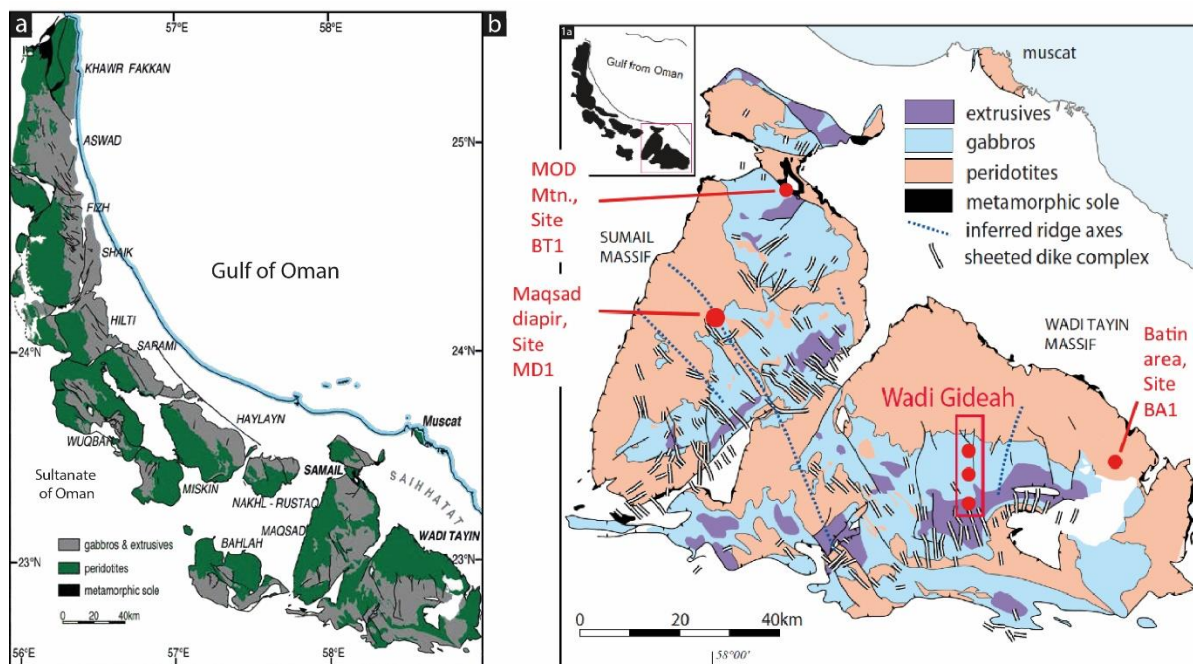

Figure 1 (a) Geological map of the Semail Ophiolite in the Sultanate of Oman and the United Arab Emirates (modified after Kelemen, 2014). (b) Map of drill sites in the Semail massif, including hole BT1, the sample location for this study (Kelemen, 2014). Inset shows the location of the study area in the Semail Ophiolite (Figure 1a).

The ophiolite was obducted along a shallowly-dipping subduction zone onto the northeastern Arabian continental margin (Figure 2) during the late Cretaceous due to the closure of the Tethys Ocean (Searle and Malpas, 1980; Coleman, 1981; Stanger, 1985; Nasir et al., 2007; Falk, 2014). Zircon ages and radiolarian cherts indicate that the Semail ophiolite was formed 97-94 Ma (Searle and Malpas, 1980; Hacker and Gnos, 1997). The timing of emplacement has been determined at 86-83 Ma by K-Ar cooling ages on biotites in greenschist facies rocks (Allemann, 1972) and at 95-89 Ma by Ar ages on hornblende in amphibolites (Lanphere, 1981), both from the metamorphic sole. Due to emplacement of the ophiolite onto the Arabian continent, the stratigraphy was tilted and eroded, exposing large sections of oceanic crust and upper mantle peridotites and harzburgites (Searle and Malpas, 1980; Stanger, 1985; Falk, 2014; Searle et al., 2015). The stratigraphy of the ophiolite succession is largely intact and includes

5

mantle sequence peridotites, layered gabbro, sheeted dikes, basaltic pillow lavas and marine sediments (Searle and Malpas, 1980; Coleman, 1981; Rioux et al., 2013).
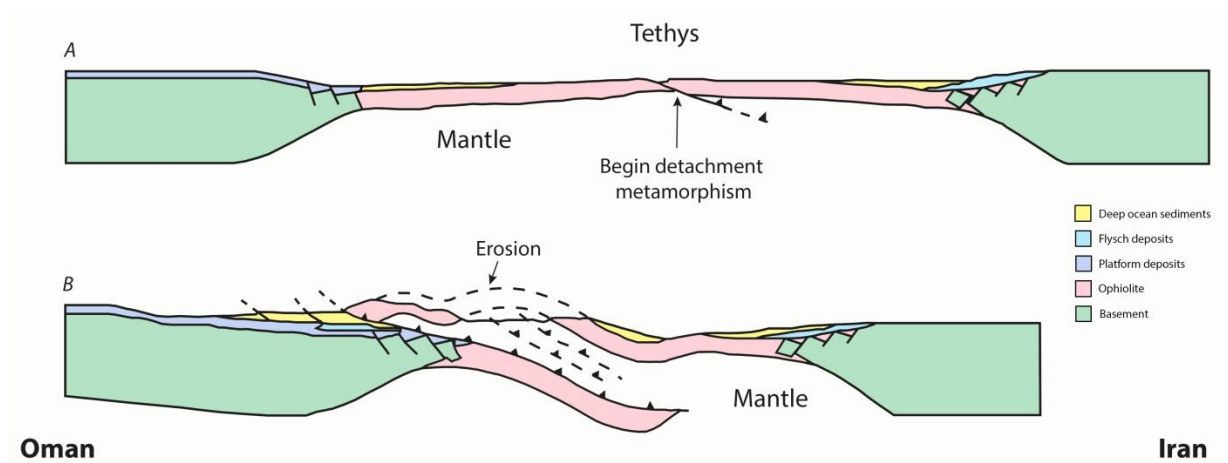

Figure 2 Schematic diagrams displaying the detachment and emplacement of the Semail ophiolite. A) Detachment of the ophiolite during closure of the Tethys Ocean as the Arabian continental margin moves northward. B) Emplacement of the Semail ophiolite along a shallowly north-dipping subduction zone due to the continued closure of the Tethys Ocean, leading to underthrusting of oceanic and continental material. Extensive erosion exposes the ophiolite at the surface (modified after Coleman (1981)).

The Semail nappe is the stratigraphically highest tectonic member in a series of allochthonous thrust sheets and is bounded by an upper cumulate zone, dominated by gabbro, and an imbricate basal thrust zone or metamorphic sole, which have both permitted fluid inflow and interaction with the rocks, resulting in extensive serpentinization (Coleman, 1981; Stanger, 1985; Nasir et al., 2007; Searle et al., 2015). The thrust fault beneath the Semail nappe separates the ophiolitic sequence from the underlying Haybi Complex (embodying the metamorphic sole in Hole BT1B) and Hawasina Complex (Figure 3) (Searle and Malpas, 1980; Coleman, 1981; Nasir et al., 2007; Rioux et al., 2013; Falk, 2014). The Haybi Complex directly underlies the Semail thrust and is composed of a series of imbricated rocks, including a sedimentary melange, volcanic rocks, limestones and serpentinites. Another major thrust separates this sequence from the relatively unmetamorphosed Hawasina Complex, which consists of pelagic sedimentary deposits formed in the Tethys Ocean (Searle and Malpas, 1980; Coleman, 1981; Falk, 2014). The Haybi and Hawasina Complexes have been thrusted over the autochthonous continental slope sediments and carbonate deposits, which overlie the pre-Permian crystalline basement (Glennie et al., 1974; Falk, 2014).
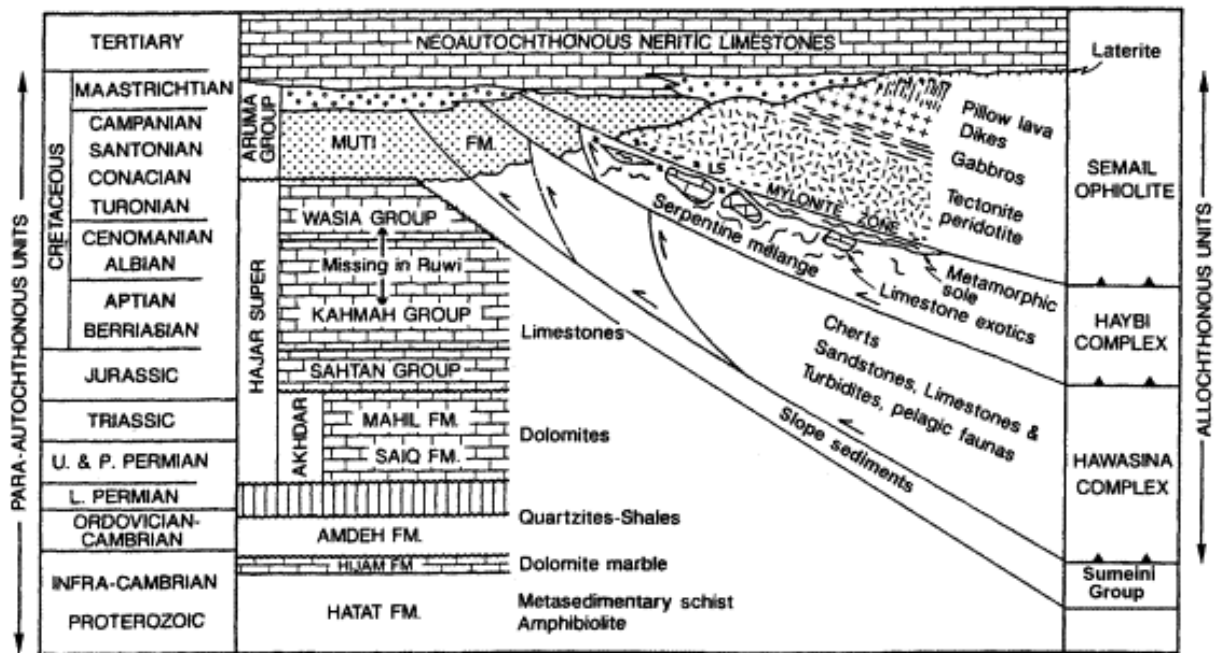
Figure 3 Stratigraphic and structural stacking of allochthonous thrust sheets in the Oman Mountains (after Glennie et al. (1974) and Nasir et al. (2007)).

3. Methods

The mineralogical composition and detailed photomicrographs of polished thin sections were obtained with the Nikon Eclipse LV100N POL polarizing microscope and DS-Fi2 camera at Curtin University. Overview scans were made using the Zeiss Axio Imager M2M at Curtin University. Back-scattered electron (BSE) images and compositional maps of polished thin sections were obtained using the Hitachi TM3030 Tabletop Microscope with the SwiftED3000 Energy Dispersive X-ray (EDX) spectrometer at Curtin University. High resolution images and more detailed compositional maps were obtained with the FEI Verios XHR scanning electron microscope (SEM) and the TESCAN VEGA3 SEM, combined with AZtec software for EDX mapping, at the Centre for Microscopy, Characterisation and Analysis (CMCA) at the University of Western Australia (UWA). Raman spectroscopy of polished thin sections was performed using the WITEC alpha 300RA+ at CMCA, UWA, in order to determine the species of carbonate found in ophicarbonates. X-ray micro CT scanning of 3.8 mm thick drill cores from thin section billets was performed by the Zeiss VersaXRM-520 at CMCA, UWA, to study the shape and distribution of carbonate spherules in three dimensions. The 3D reconstruction of the scans was made with Avizo for FEI software. A focused ion beam (FIB) cut of a carbonate spherule was made with the FEI Helios Nanolab G3 CX DualBeam equipped with FIB technology and studied with transmission electron microscopy (TEM) using the FEI Titan G2 80-200 TEM/STEM at CMCA, UWA. Automated mineralogy was performed with the TESCAN Integrated Mineral Analyser (TIMA) at the Digital Mineralogy Hub (DMH), John de Laeter Centre (Curtin University), in order to determine mineral distribution and grain size.

Quantitative elemental maps and mineral compositions were acquired on a JEOL 8530F electron probe micro analyser (EPMA) housed at CMCA, UWA. The EPMA is equipped with 5 tunable wavelength dispersive spectrometers. Operating conditions were 40 degrees takeoff angle, and a beam energy of 15 keV. Carbonate analyses were conducted using a beam current of 15 nA for calibration and map acquisition. The beam diameter was 5 µm for spot analysis and quantitative element maps were acquired with a fully focused beam. Dwell time was 100 msec per pixel with a pixel dimension of 1×1 µm. For spot analyses element concentrations were acquired using analysing crystals LiFH for Pr Lα1, Sm Lα1, Yb Lα1, LiF for Eu Lα1, Fe Kα1, Gd Lα1, La Lα1, Mg Kα1, Mn Kα1, PETJ for Ba Lα1, Ca Kα1, Sr Lα1, and TAP for Ce Lα1. For quantitative maps, element concentrations were acquired using analysing crystals LiFH for Fe Kα1, LiF for Gd Lα1, PETJ for Ca Kα1 and TAP for Mg Kα1. Silicate analyses were conducted with a 15nA beam current for calibration and map acquisition and a 5 µm beam diameter for spot analysis. For spot analyses element concentrations were acquired using analysing crystals LiF for Ni Kα1, Mn Kα1, Fe Kα1, Cr Kα1, Ti Kα1, PETH for Ca Kα1, K Kα1, Cl Kα1, TAP for Mg Kα1, Na Kα1, Si Kα1, Al Kα1.

The standards were an assortment of synthetic and natural minerals and metals. The counting time was 20 seconds on peak for all elements, and Mean Atomic Number background corrects were used throughout (Donovan and Tingle, 1995). The intensity data was corrected for Time Dependent Intensity (TDI) loss (or gain) using a self–calibrated correction for Si Kα1, Na Kα1, Ti Kα1, K Kα1, Fe Kα1. Interference corrections were applied to Fe for interference by Mn, and to Mn for interference by Cr (Donovan et al., 1993). Results are the average of 3 points and detection limits ranged from 0.013 wt% for Si Kα1 to 0.012 wt% for Mg Kα1 to 0.033 wt% for Fe Kα1 to 0.011 wt% for Ca Kα1 to 0.04 wt% for Ni Kα1. Oxygen and carbon were calculated by cation stoichiometry and included in the matrix correction. The elemental maps were processed using Probe Software's CalcImage application and Matlab. The matrix correction method was ZAF and the mass absorption coefficients dataset was LINEMU Henke (LBL, 1985) < 10KeV / CITZMU > 10KeV. The ZAF algorithm utilised was Armstrong/Love Scott (Armstrong, 1988).

4. Results

A total of fifteen thin sections were prepared from the Oman ophiolite, representing the transition from upper listvenite to serpentinite and ophicarbonate, to lower listvenite and the basal thrust. The locations of samples used for thin section preparation along the BT1B drill core are indicated in Figure 4.
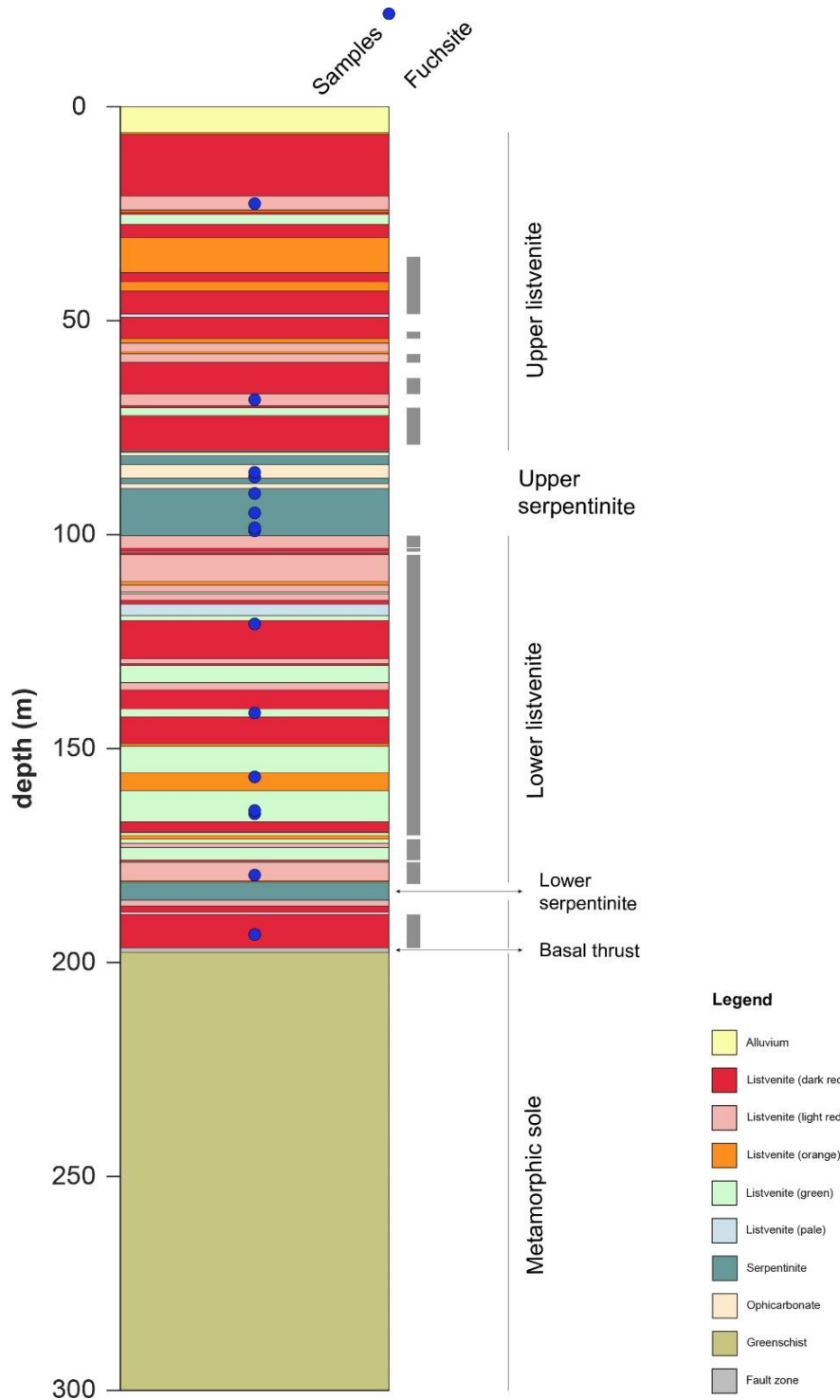

Figure 4 Stratigraphic column of Hole BT1B, including locations of samples and presence of fuchsite. Information about lithology is taken from the Oman Drilling Project.

4.1 Bulk rock composition

Whole rock chemical analyses were performed on 44 listvenites, ophicarbonates and serpentinites, and 13 metamorphic sole samples during the shipboard core logging activity of the Oman Drilling Project Phase 1 Science Team (2019) on board D/V Chikyu (Site BT1 in Kelemen et al., 2019 in prep). Select major and trace element compositions are displayed in Figure 5. All element concentrations, with the exception of Al_2O_3, are highly variable in both listvenites and ophicarbonate/serpentinite sequences, and do not show any clear trends. The transition from the altered ophiolitic mantle to metamorphic sole, however, is characterized by a sharp change in measured compositions, except for CaO. The lower listvenite displays a slight enrichment in Sr and CaO toward the basal thrust and metamorphic sole. The listvenites, ophicarbonates and serpentinites display a broad range of values for Loss on Ignition (LOI), varying from 15.23 to 42.6 wt%. The SiO_2/MgO ratio and Mg# remain constant throughout the altered ophiolitic sequence.

4.2 Mineralogy and petrology

Optical microscopy, Raman spectroscopy, back-scattered electron (BSE) imaging and electron microprobe analysis reveal the characteristic mineralogy of the different rock types found in Hole BT1B, extensive veining networks and crosscutting relationships, and the presence of carbonate spherules. A list of the samples and their mineral assemblages is presented in Table S1.

4.2.1 Upper listvenite

The upper listvenites are red in hand specimen and have a very fine grained, brecciated carbonate matrix with fine grained quartz and oxides (Figure A1). The samples contain minor hematite and chromite. Hematite occurs as a fine grained phase, often intergrown with quartz (Figure 6a) or magnesite (Figure 6b) in quartz-carbonate veins. Magnesite mostly occurs as the main constituent of the fine-grained matrix, but also makes up coarser grained (quartz-)carbonate veins. The euhedral magnesite grains in these veins occasionally display an oscillatory zoning pattern (Figure 6b, c). Several sets of magnesite veins (10-50 µm) cut the quartz-carbonate matrix, and occasionally contain small oxides. These are crosscut by coarser grained, magnesite veins (50-300 µm), which are in turn intersected and occasionally replaced by quartz(-magnesite) veins (50-300 µm) (Figure 6f). Coarse grained dolomite veins (100-300 µm) crosscut the magnesite and quartz veins (Figure 6d-f).
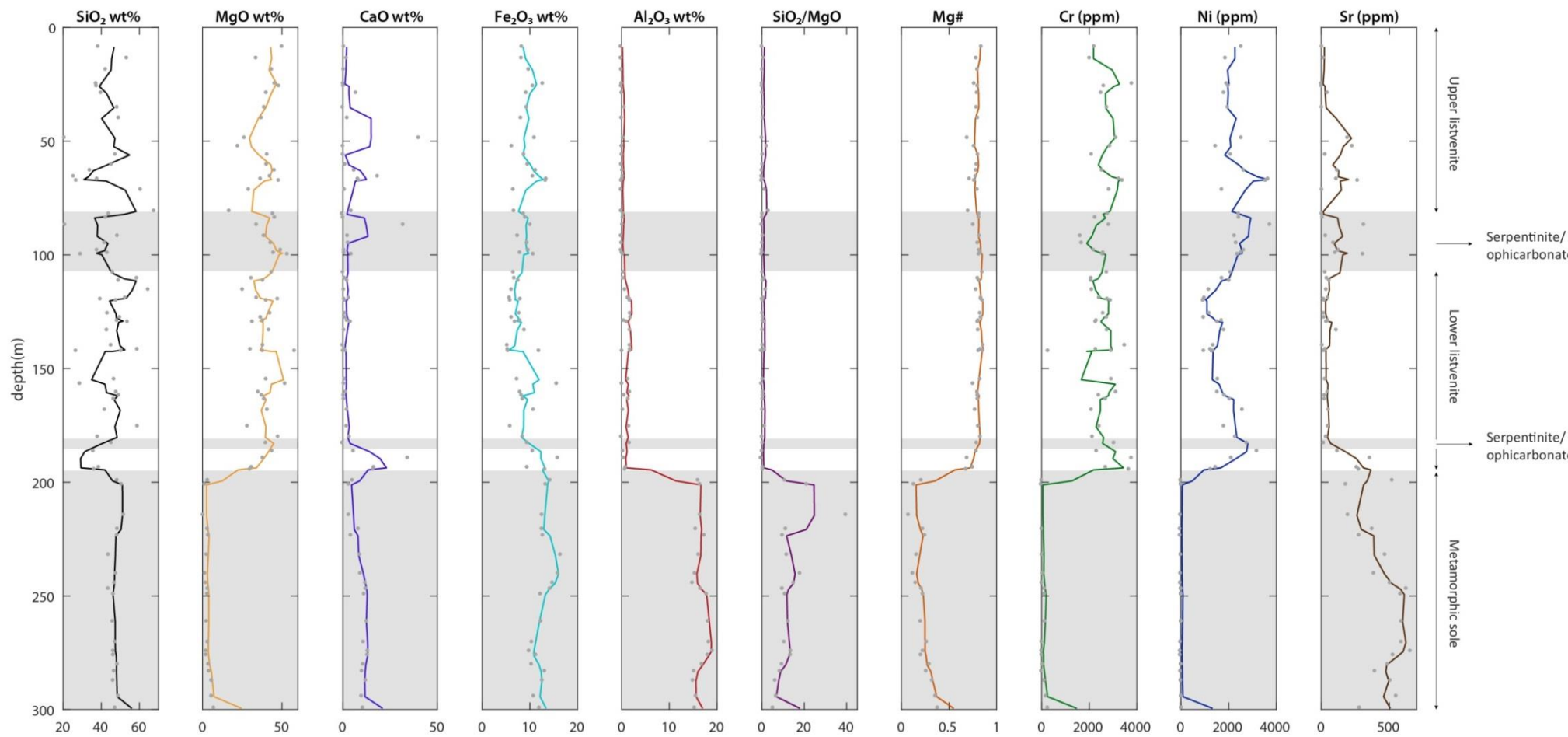
Figure 5 Bulk rock composition with depth in BT1B, indicated with three point moving average. Different lithologies (listvenite, serpentinite/ophicarbonate and metamorphic sole) are indicated.
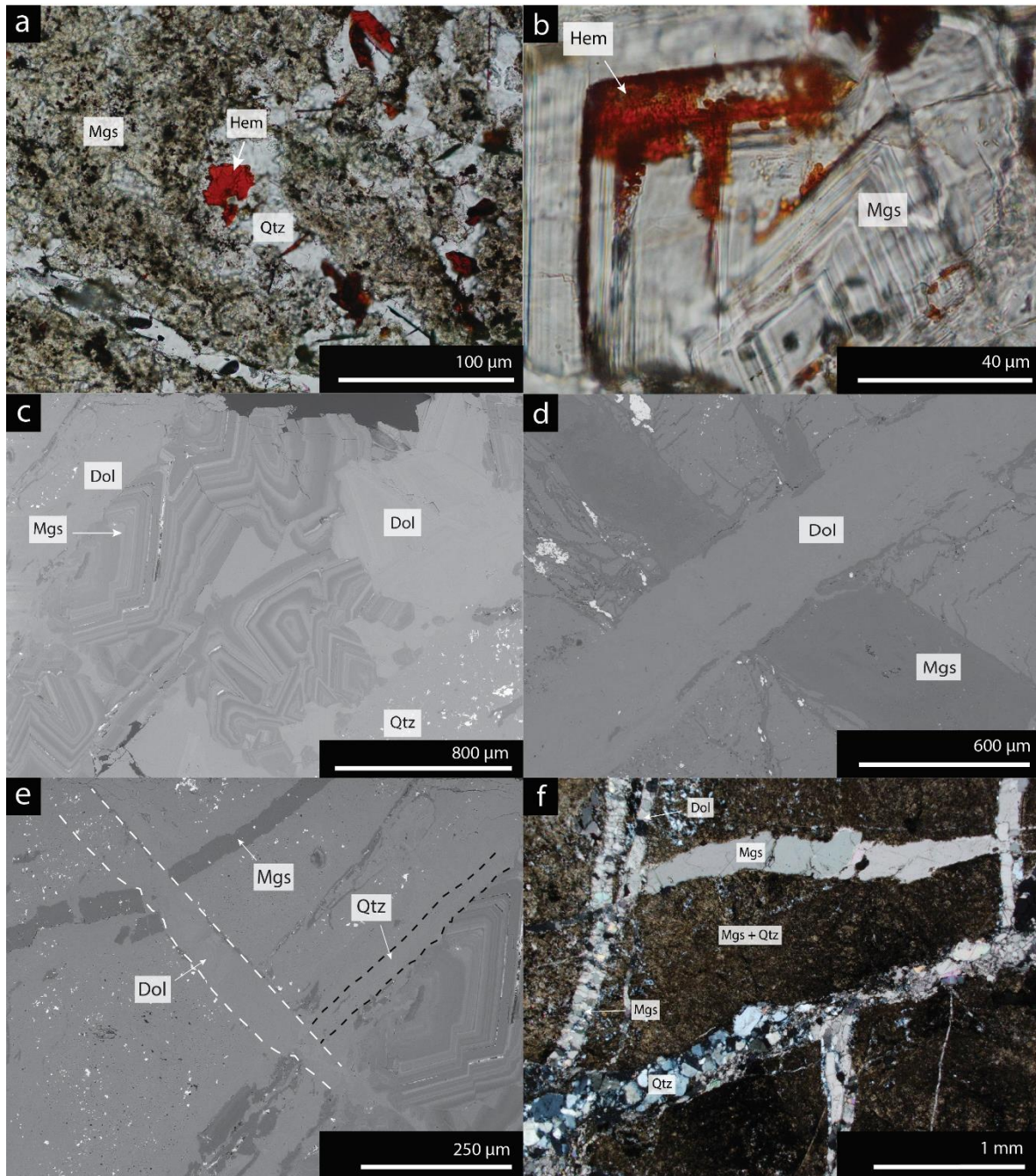
Figure 6 (a) Photomicrograph of hematite intergrown with quartz in a fine grained quartz-magnesite matrix, sample 13-02-73-77 (plane polarized light, PPL). (b) Photomicrograph of hematite intergrown with magnesite, which shows oscillatory zoning, sample 32-02-22-26 (PPL). (c) Back-scattered electron (BSE) image of quartz-carbonate vein in sample 32-02-22-26, containing minor hematite intergrown with zoned magnesite, dolomite and quartz. (d) BSE image of cross-cutting relationship between magnesite and dolomite vein in sample 32-02-22-26. Dolomite intersects magnesite vein, which cuts through fine grained carbonate matrix. (e) BSE image of cross-cutting relationships between several sets of veins, sample 32-02-22-26. Magnesite and quartz veins are crosscut by dolomite vein. (f) Photomicrograph of cross-cutting relationships between several sets of veins, sample 13-02-73-77. Magnesite veins cut through fine grained magnesite quartz matrix and are intersected and replaced by dolomite veins. These are cut by quartz-carbonate veins (cross polarized light, XPL).

4.2.2 Serpentinite and ophicarbonate

The uppermost sample of this lithology (39-04-68-72) can be classified as serpentinite due to the small amount of carbonate present (Figure A2). However, the carbonate concentration increases with depth and additional samples from this serpentinite layer are thus classified as ophicarbonates. These samples contain serpentine, magnesite, dolomite, minor Cr-spinel and relicts of orthopyroxene (bastite). The matrix of the serpentinite and ophicarbonates varies from purely serpentine to a mixture of very fine grained serpentine and carbonate. In some samples, the characteristic mesh texture originating from serpentinization of olivine can still be recognized (Figure 7a), but the samples do not contain any olivine relicts. The serpentine matrix is cut by relatively thin serpentine veins (10-50 µm), which are crosscut by carbonate veins or a second generation of serpentine veins (100-200 µm) (Figure 7b). These veins pose as an easy fluid pathway for later generations of fluid, and are thus sometimes partly replaced by magnesite (Figure 7a). With increasing depth, the concentration of magnesite veins increases (Figure 7c, d), which crosscut serpentine veins and replace relicts of orthopyroxene. Within the sample closest to the lower ophicarbonate-listvenite transition, the magnesite veins show a decrease of the iron concentration towards the edges of the vein (Figure 7d).

Aside from carbonate veins, the lowermost ophicarbonates (samples 44-01-8-13 and 44-03-60-63) also contain carbonate spherules (Figure 8). The spherules have approximately the same diameter (~50 µm) and are mostly concentrated around carbonate veins (Figure 8a). They either appear as single phases, or in small clusters (Figure 8b), where the spherules have clearly accumulated but can still be recognized as the original features. Upon closer inspection, the carbonate spherules display an inner chemical zonation due to the occurrence of different kinds of carbonate. EDX mapping and electron probe microanalysis (Table S2) show that the core of the spherules is enriched in Mg and the concentration of Fe increases towards the rim. The rim itself is enriched in Ca and Mn, whereas the Mg-rich serpentine matrix is completely devoid of Ca (Figure 9, 10, 12). Even though the spherules have clustered together, the original inner zonation can still be recognized. Raman spectroscopy confirms that the cores of the carbonates are composed of magnesite, whereas the rim is composed of dolomite (Figure 11). In some examples, this concentric variation of magnesite and dolomite is repeated once or twice more. The carbonate spherules contain several inclusions comprising Fe-oxides, serpentine and spinel.

Electron probe microanalysis (Table S3) demonstrates that the serpentine matrix contains a serpentine vein network, in which the serpentine veins have a lower Fe concentration (1 wt%) than the matrix serpentine (6 wt%). Transmission electron microscopy shows that the porosity in the serpentine matrix around the carbonate spherules is distinct compared to the magnesite rim, which is very homogeneous (Figure 12).
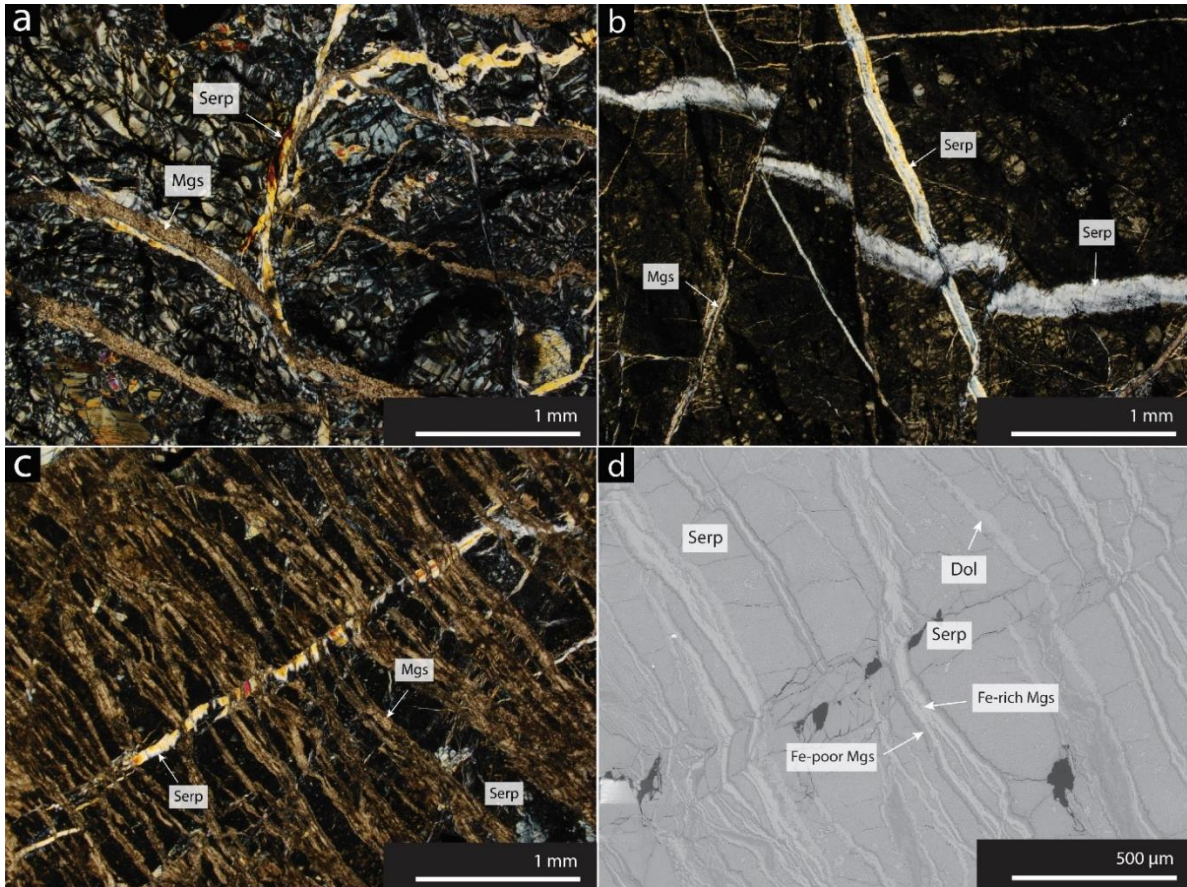
Figure 7 (a) Photomicrograph of magnesite vein crosscutting and replacing serpentine vein in sample 39-04-68-72. Mesh texture is clearly visible in matrix of the sample (XPL). (b) Photomicrograph of serpentine vein crosscut by a later serpentine vein, in turn crosscut and offset by magnesite veins in sample 41-04-25-29 (XPL). (c) Photomicrograph of a serpentine vein crosscut by an extensive network of later carbonate veins, sample 44-03-60-63 (XPL). (d) BSE image of serpentine vein crosscut by carbonate (magnesite, dolomite) veins, sample 44-03-60-63. Magnesite veins show a variation in iron concentration, which decreases towards the edge of the vein.
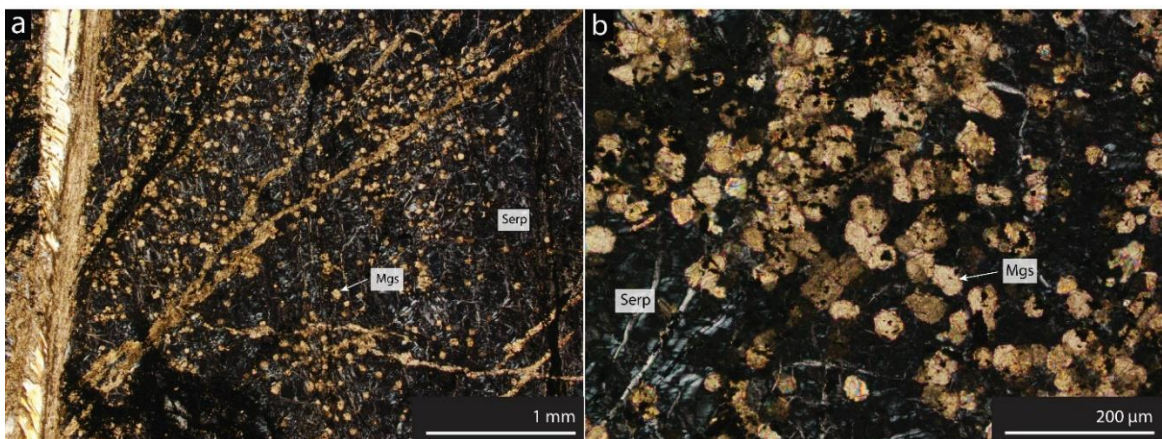

Figure 8 (a) Photomicrograph of ophicarbonate containing carbonate spherules, sample 44-01-08-13. Concentration of spherules is highest around carbonate vein on the left of the image, and decreases away from the vein (XPL). (b) Close-up photomicrograph of carbonate spherules within sample 44-01-08-13. Spherules appear as single features or as clusters (XPL).
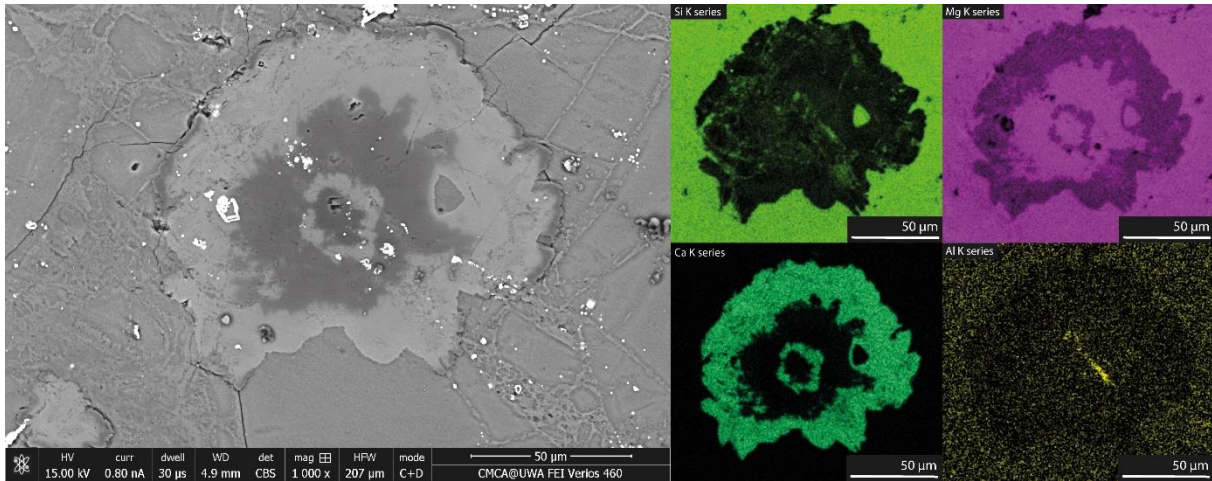
Figure 9 BSE image and element compositional maps of single carbonate spherule within ophicarbonate, sample 44-01-08-13. The spherule has a Mg-rich core and Ca-rich rim, followed by another sequence of Mg-rich and Ca-rich carbonate. In some places, the spherule shows a last, outer, rim of Mg-rich carbonate. Inclusions consist of oxides, serpentine, and spinel (Al-rich phase).
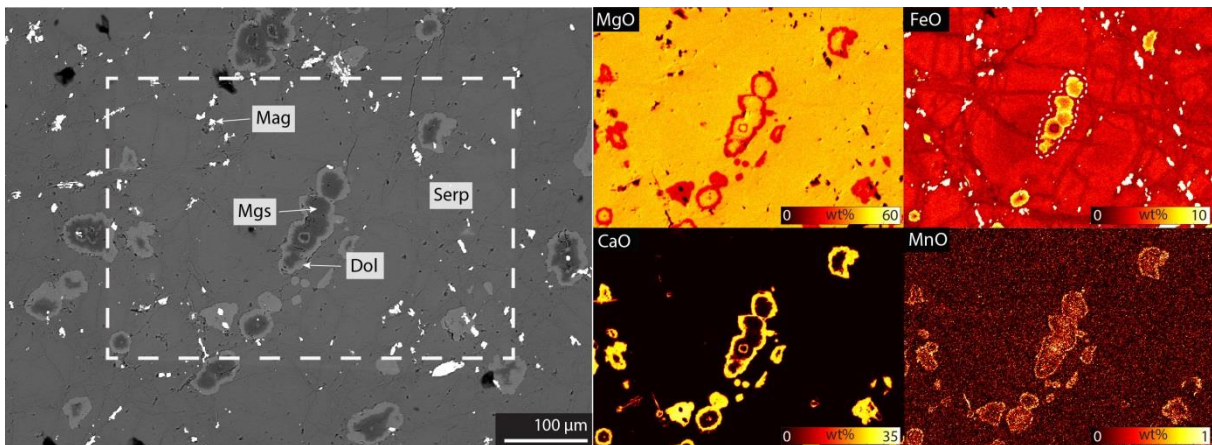
Figure 10 BSE image and microprobe elemental maps (for MgO, FeO, CaO and MnO) of carbonate spherules within ophicarbonate (sample 44-01-08-13). White dashed inset in BSE image shows location of elemental maps. Spherules have clustered together, but still show some inner zonation associated with separate carbonate spherules. The core is enriched in MgO, and shows an increase in FeO towards the rim, whereas the rim itself is enriched in CaO and MnO. The matrix of the sample consists of serpentine, which shows a clear variation in its FeO contents.
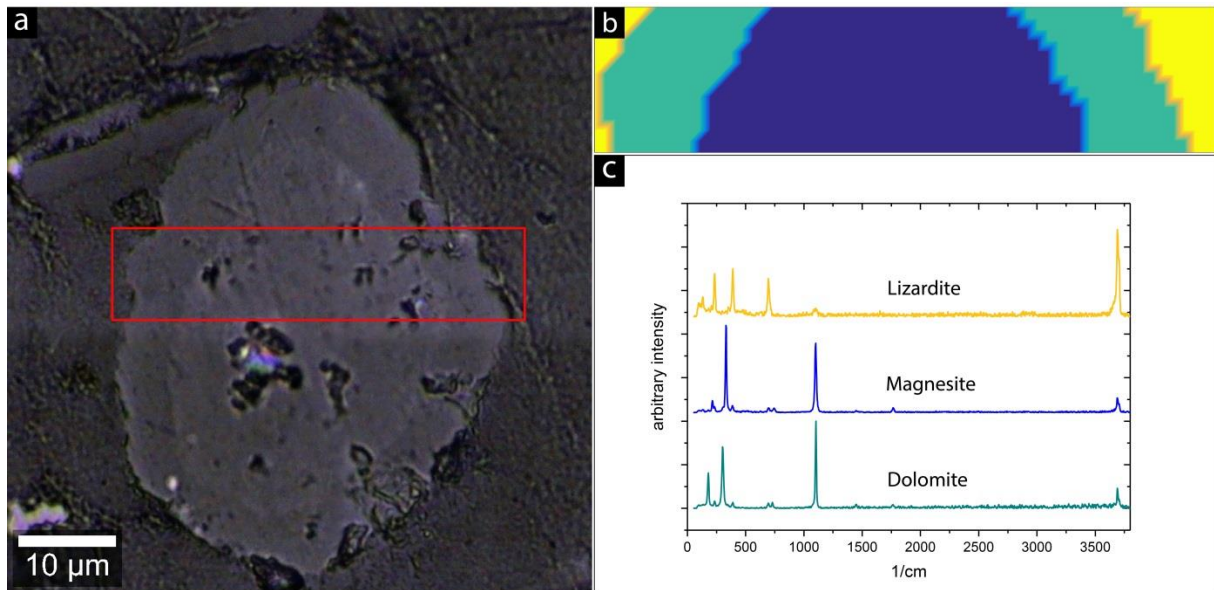
Figure 11 (a) Reflected light image of a single carbonate spherule within ophicarbonate (sample 44-01-08-13). Red box shows the location of Raman principal component analysis map displayed in 1b. (b) Raman principal component analysis map. (c) Average Raman spectra for the three components of the PCA map indicating the presence of lizardite, magnesite and dolomite. Colours correspond to the components in 1b.
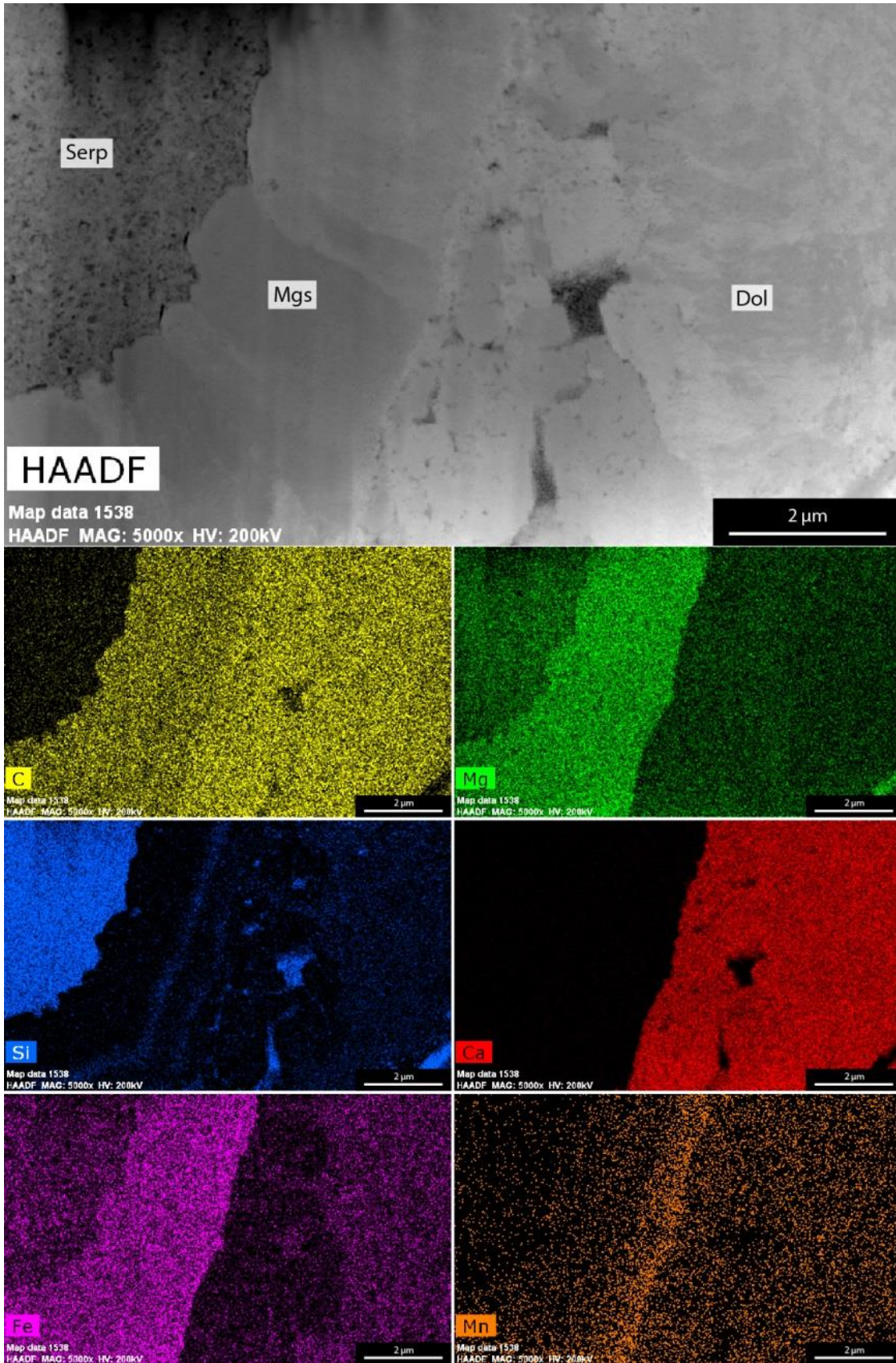
Figure 12 TEM micrograph of carbonate rim and serpentine matrix (sample 44-01-08-13) and STEM-EDS maps for C, Mg, Si, Ca, Fe and Mn. Magnesite and dolomite are very homogeneous, whereas serpentine matrix is fine grained and porous. Dolomite contains several inclusions of serpentine.

4.2.3 Lower listvenite

The lower listvenites appear green in hand sample and generally have a matrix of fine to coarse grained carbonate and fine grained quartz (Figure A3). The characteristic green colour of the rocks is caused by the presence of minor fuchsite (Figure 13a), which is often intergrown with quartz and carbonate, or associated with relicts of Cr-spinel. Several sets of carbonate veins can be recognized in the lower listvenites. At least two generations of magnesite veining are identified due to crosscutting relationships. The magnesite veins (10-50 µm) are crosscut by quartz-carbonate veins (~300 µm) and coarse grained dolomite veins (~500 µm) (Figure 13b). Several coarse grained magnesite veins (800 µm – 1 mm) are antitaxial, and display a clear median zone and elongated crystals (Figure 13c). In sample 65-01-5-9, one extremely thick quartz vein (1.5 mm) occurs, which is offset and heavily deformed (Figure 13d). It is apparent from the preserved texture and cleavage that this quartz vein pseudomorphically replaced an earlier serpentine vein. The quartz vein contains thin fractures and veins (~50 µm) that are either filled up with fine grained quartz or with coarser grained carbonate, that texturally resemble the carbonate spherules described in the ophicarbonate. The carbonates are aligned along the cleavage direction of the precursor serpentine, whereas the quartz cuts randomly through the vein.

Like the lower ophicarbonates, the upper green listvenites (52-01-41-46 and 60-03-29-33) contain carbonate spherules (Figure 14). These are bigger than their counterparts in the ophicarbonates (~100 µm) and occur as isolated grains (Figure 14a, b) and clusters composed of several amalgamated spherulites (Figure 14c, d). These carbonate spherules show the same chemical zonation as the ones found in the ophicarbonates. However, Raman spectroscopy shows that the outer rim is composed of Ca-rich magnesite instead of dolomite. Electron probe microanalysis (Table S2) indicates that the core of the spherules is enriched in Mg, whereas the rim is enriched in Ca and Fe (Figure 15).
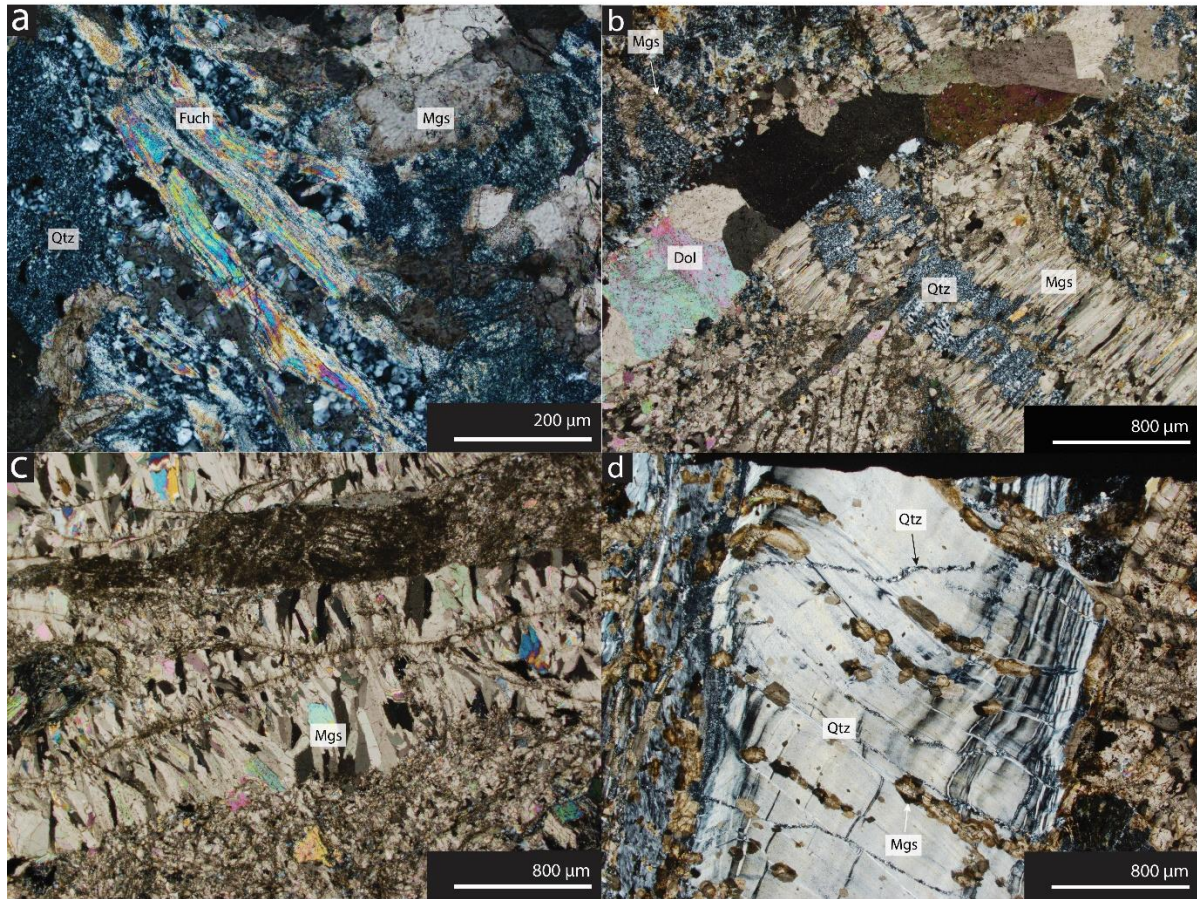
Figure 13 (a) Photomicrograph of fuchsite intergrown with quartz in sample 65-01-05-09. Only minor fuchsite gives the rock its striking green colour (XPL). (b) Antitaxial magnesite vein, associated with fine grained quartz, crosscut by a thick, coarse grained dolomite vein in sample 52-01-41-46 (XPL). (c) Photomicrograph of antitaxial magnesite vein with clear median zone and elongated carbonate crystals, within fine grained magnesite matrix of sample 68-02-14-18 (XPL). (d) Photomicrograph of a quartz vein that pseudomorphically replaced a serpentine vein in sample 65-01-05-09. Magnesite grains have filled up cracks that follow the cleavage of the serpentine, whereas thin quartz veins cut randomly through the thick quartz vein (XPL).

The green listvenites contain several carbonate spherules that have been overgrown by zoned, euhedral carbonate (Figure 16). Electron probe microanalysis (Table S2) shows that the pre-existing spherules and euhedral overgrowths differ in their chemical compositions. The spherules are lower in Ca and Fe concentration compared to the euhedral rim. The concentration of Fe in the overgrowth decreases away from the core, whereas the Ca concentration increases toward the outer rim.

A strong variation in Fe and Ca concentration can also be seen in most veins within the listvenites, especially antitaxial veins as seen in Figure 13c. A line scan taken across one of these veins with the electron microprobe is shown in Figure 17. The median line is enriched in Mg and depleted in Fe, Mn and Ca, but these concentrations change abruptly inside the vein itself. Fe, Mn and Ca concentrations are exceptionally high in the centre of the vein and decrease toward the vein rim, whereas the

concentration of Mg increases away from the vein centre. A small increase in Mg concentrations and decrease in Fe and Mn concentrations is caused by a number of pure magnesite inclusions.
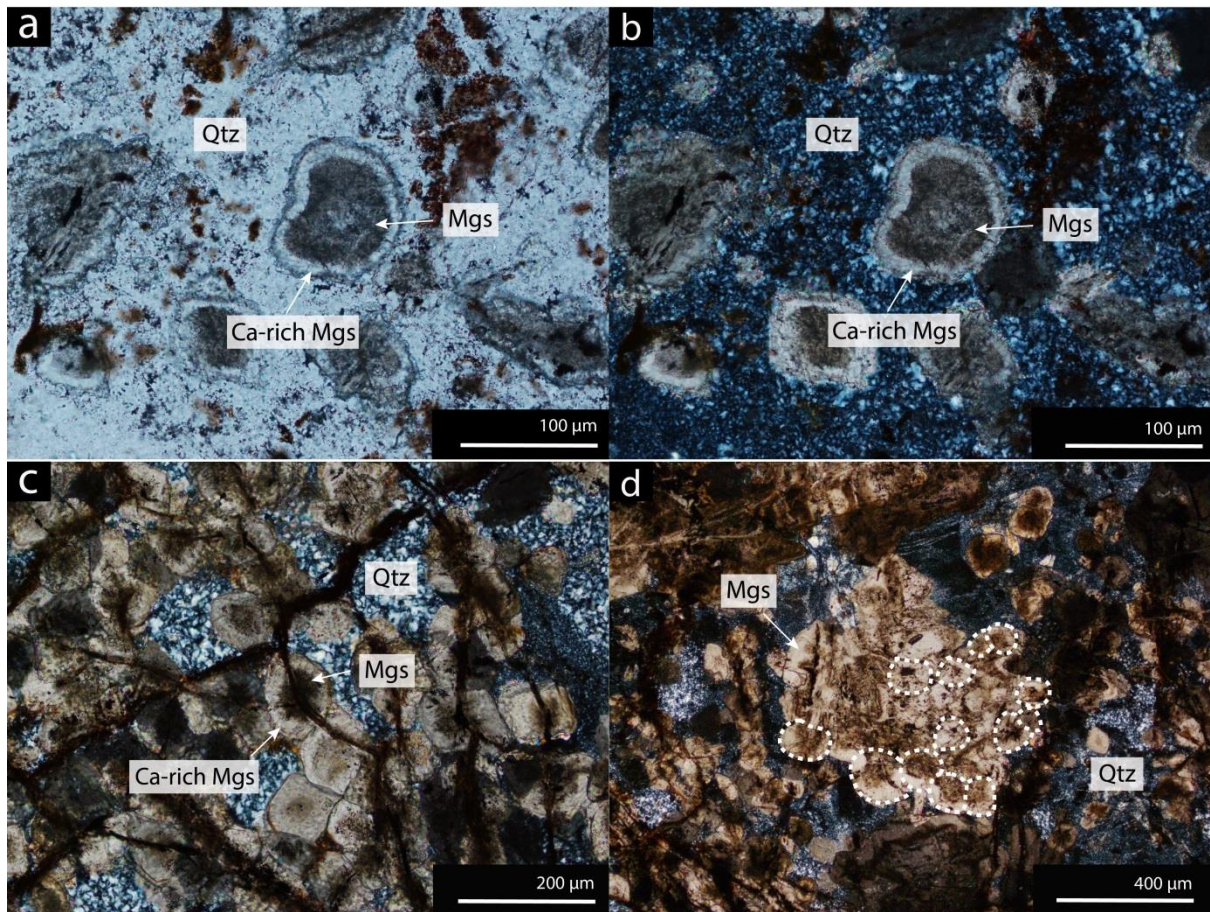
Figure 14 (a) and (b) Photomicrograph of carbonate spherule within a fine grained quartz matrix in a listvenite, sample 60-03-29-33. The core is composed of magnesite, whereas the rim consists of Ca-rich magnesite (PPl and XPL). (c) Photomicrograph of carbonate spherules with inner chemical zonation clustered together, grain boundaries have coalesced, sample 60-03-29-33 (XPL). (d) Photomicrograph of accumulation of several carbonate spherules, grain boundaries are not visible anymore, sample 60-03-29-33 (XPL).
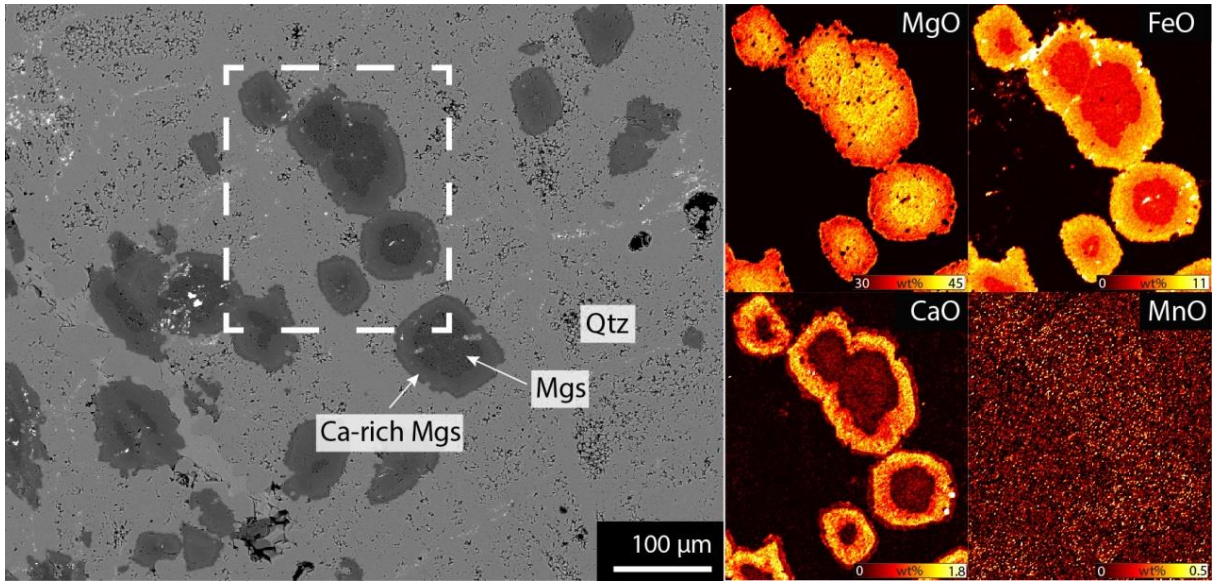
Figure 15 BSE image and microprobe elemental maps (for MgO, FeO, CaO and MnO) of carbonate spherules within listvenite (sample 60-03-29-33). White dashed inset in BSE image shows the location of elemental maps. Some spherules have clustered together, causing the inner zonation to disappear completely. The core of the spherules is enriched in MgO and slightly depleted in FeO compared to the rim. The rim itself is enriched in CaO, whereas the thin outer rim displays the same composition as the core of the spherule. MnO seems to be slightly enriched within the spherule compared to the quartz matrix, but detection limits are too low to provide information about differences between core and rim.
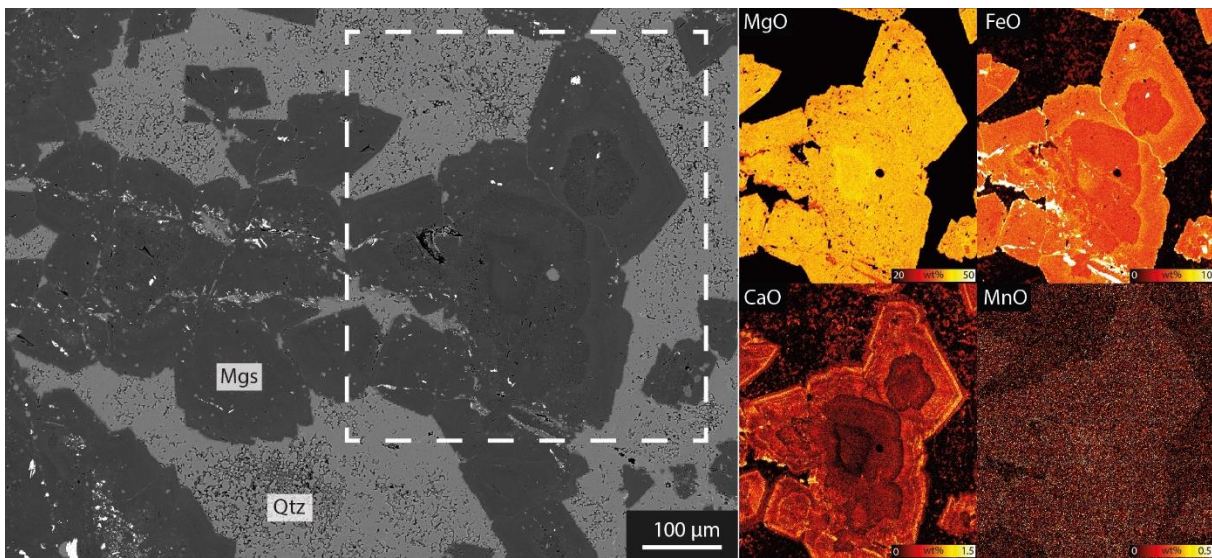
Figure 16 BSE image and microprobe elemental maps (for MgO, FeO, CaO and MnO) of euhedral, zoned carbonate within listvenite (sample 60-03-29-33). White dashed inset in BSE image shows location of elemental maps. The carbonates displayed in the elemental maps show a clear inner zonation, characterised by a variation in FeO and CaO. The core is relatively depleted in FeO and CaO, whereas the euhedral overgrowth is enriched in both. The concentration of FeO decreases away from the core, whereas the CaO concentration increases towards the outer rim.
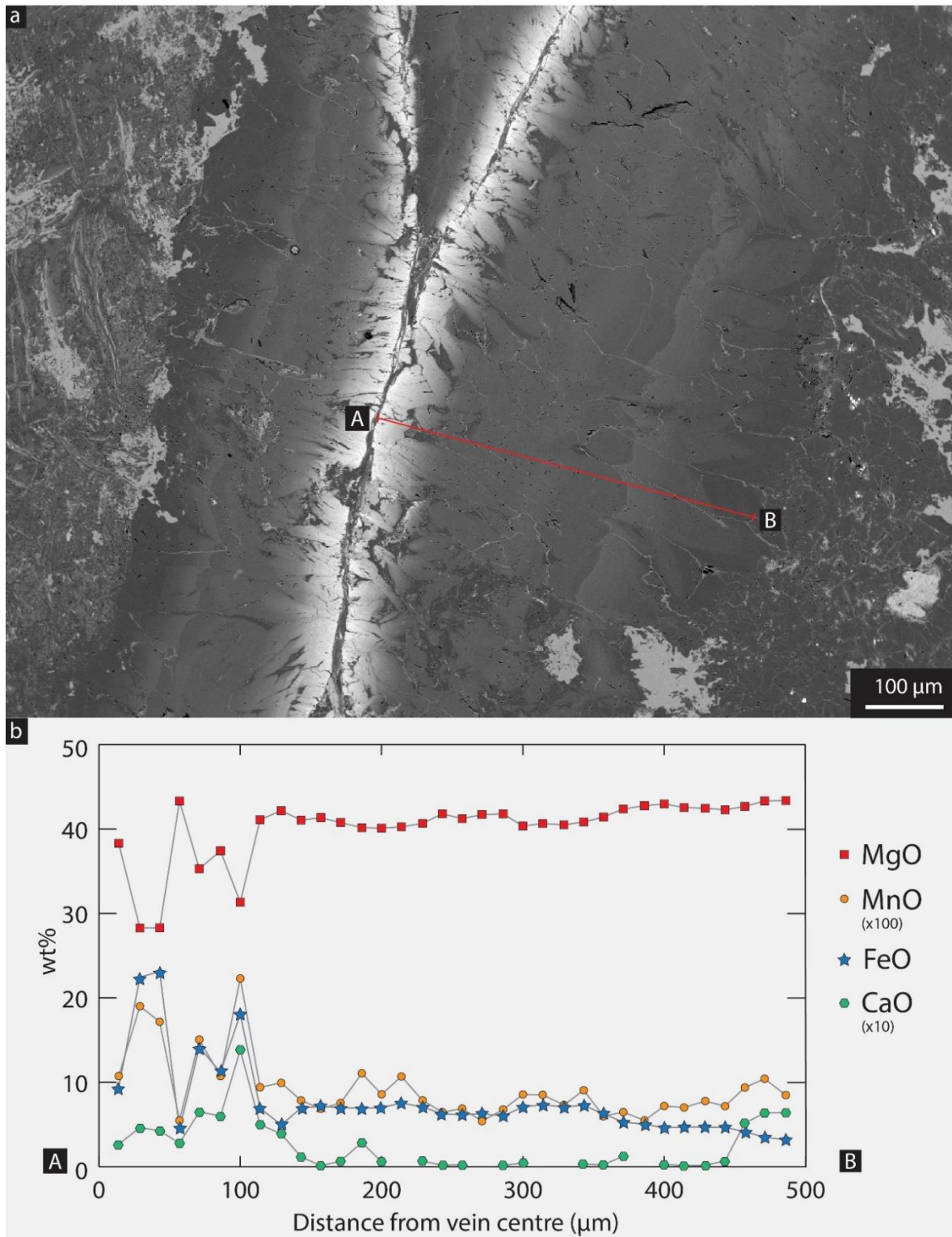
Figure 17 (a) Position of electron microprobe line scan, perpendicular to the veining direction (sample 68-02-14-18). (b) MgO, MnO (x100), FeO, CaO (x10) concentrations in wt% plotted against distance from the antitaxial vein centre. Positions A and B correspond to the positions in (a). The concentration of MgO increases away from the vein centre, whereas the concentrations of MnO, FeO and CaO follow the same trend and decrease toward the vein rim. The vein centre is clearly enriched in MnO, FeO and CaO, with the exception of the MgO-rich median line and a number of FeO and MnO depleted inclusions within the vein. Disruptions in the concentration of CaO indicate values below the detection limit.

4.2.4 Basal thrust

The lowermost sample (77-03-11-15) was taken in close proximity to the basal thrust beneath the Oman ophiolite. The sample is identified as a listvenite due to the presence of both fine grained carbonate and quartz, but it is almost entirely carbonated and the amount of quartz is low. The sample shows signs of intense alteration and shearing, and contains large amounts of iron oxides (Figure 18). Several carbonate veins can be recognized, which vary in thickness and grain size.
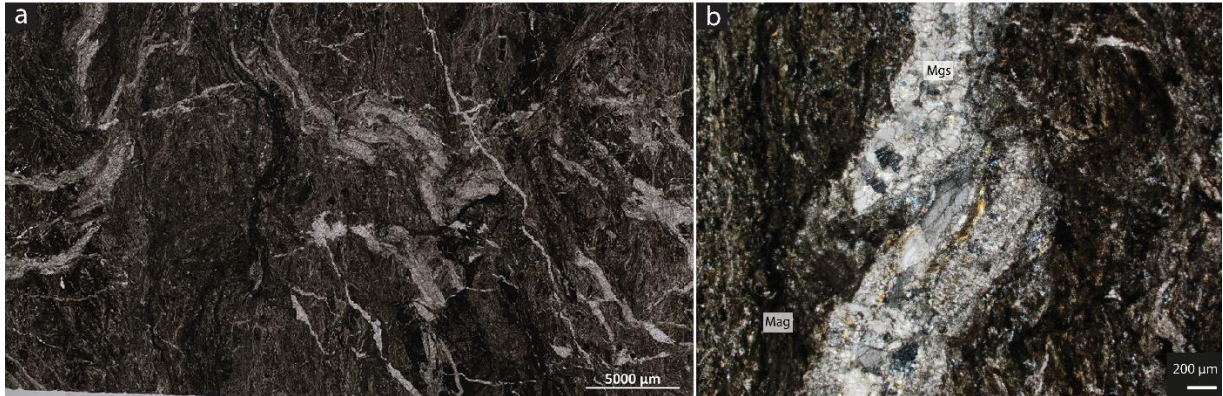
Figure 18 (a) plane polarized overview scan of sample 77-03-11-15, listvenite containing very fine grained carbonate and oxides, and minor quartz. (b) Photomicrograph of listvenite closest to the basal thrust. Magnesite vein has been heavily deformed and sheared, carbonate matrix is extremely fine grained and also severely deformed (XPL).

4.3 X-ray micro-CT scanning

A 3D reconstruction of the X-ray micro-CT scan reveals the shape and distribution of the carbonate spherules in the ophicarbonates (Figure 19). The grains are relatively uniform in shape, varying from perfect spheres to cylinder-like structures. A large amount of spherules is connected to each other by small-scale veins or by accumulation of carbonates into clusters. This creates an extensive network through the sample. The connections between carbonate spherules can be traced back to the two carbonate veins in the sample, which act as the dominant linking feature.
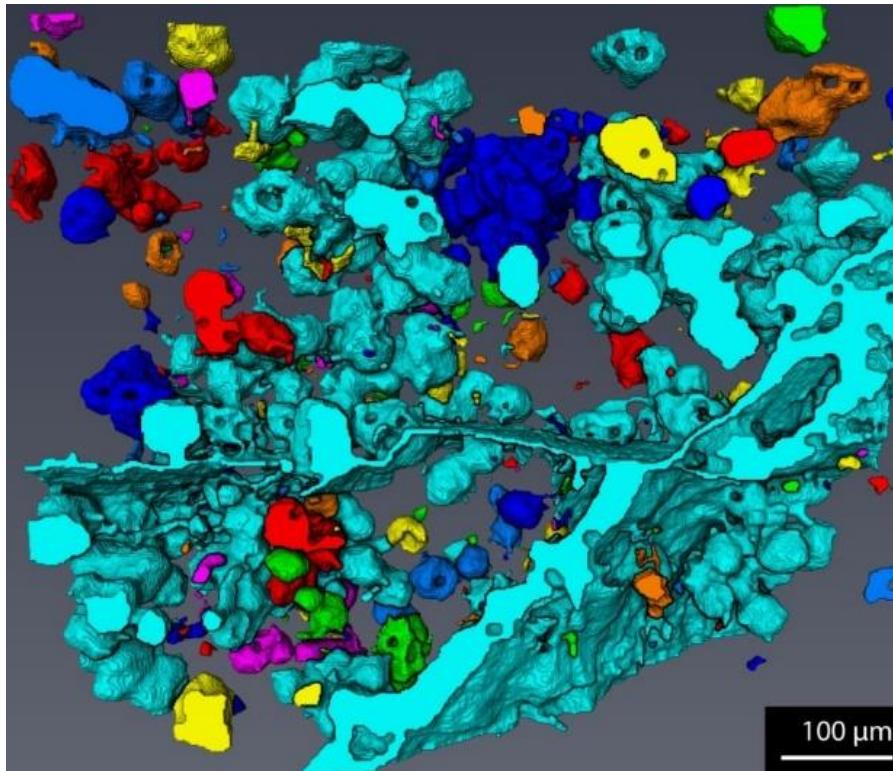
Figure 19 3D reconstruction of X-ray micro CT scan of sample 44-01-8-13, showing distinct carbonate spherules and veins. Many carbonate spherules are connected to each other and to the two carbonate veins in the sample, which act as dominant linking features.

5. Discussion

5.1 Carbonation textures

5.1.1 Veining

Although the degree of deformation and carbonation varies per sample, all the rocks display a set of compositionally varying veins. These indicate fracturing of the rock and would have posed as fluid pathways, enabling the influx of CO_2-rich fluids, leading to pervasive carbonation. The number and composition of the veins differs per sample and per lithology, but a general trend in cross-cutting relationships can be found in the rocks. The earliest veins that are observed are composed of serpentine and solely present in the ophicarbonates. These have been exposed to a certain grade of deformation since a number of veins appear to be offset or sheared. The second generation of veining includes the formation of magnesite, which either cross-cuts or replaces earlier formed serpentine. Magnesite veins are recognised as the earliest generation in listvenites. These are intersected by the third generation of veining, comprised of either pure quartz or a mixture of quartz and carbonate, followed by the youngest set of dolomite veins. Due to a lack in cross-cutting relationships, it is not entirely clear if the Fe-enriched are younger or later than the pure magnesite veins.

The veins in the ophicarbonates and listvenites do not only provide information about the timing of mineral growth through cross-cutting relationships, but also by means of replacement reactions. Quartz has been found to pseudomorphically replace serpentine (Figure 13d), whereas magnesite grains remain situated in previous cleavage planes. Later quartz veins cut randomly through the feature, independent of earlier existing textures. The listvenites display a large amount of antitaxial magnesite veins, characteristic for their median zones and fibrous crystals, both composed of magnesite as well. In this case, serpentine is replaced by magnesite, which is reflected in the fibrous morphology of the crystals, caused by the cleavage of the precursor serpentine. These relationships support the idea that quartz and magnesite veins are a later feature than serpentine veins.

Most of the antitaxial veins show distinct, consistent, variations in Fe and Mg concentrations (Figure 17). The median zone is always enriched in Mg and depleted in Fe, whereas the fibrous crystals show an increase in Mg and decrease in Fe away from the vein centre. This relationship is also observed in more fine grained veins in ophicarbonates (Figure 7d). Since the minerals in an antitaxial vein grow from the median zone outward until they reach the wall rock (Bons et al., 2012), this would implicate that the fluid from which vein material precipitated was rich in Fe and became increasingly depleted in Fe and enriched in Mg as precipitation continued.

The intensity of veining and the variety of cross-cutting relationships suggest that the alteration of these rocks progressed due to repeated influx of fluid pulses, which was likely facilitated by progressive brittle deformation.

5.1.2 Carbonate spherules

5.1.2.1 Spherule distribution

X-ray micro CT, SEM imaging and automated mineral phase mapping indicate that the carbonate spherules are evenly distributed and all have the same size, suggesting that they were formed during one event and grew for the same amount of time. The spherules are also concentrated around carbonate veins, where they are mostly connected to each other to form a network of spherical particles. Further away from the vein, the carbonate spherules start to appear as isolated grains. Automated mineralogy produced a compositional map of one of the ophicarbonate samples, showing all the present phases including the carbonate spherules containing both magnesite and dolomite (Figure 20a). After removing the non-carbonate phases and the veins, a particle density map could be made that shows the area fraction of carbonate and the number of carbonate nuclei per mm^2 (Figure 20b). This map supports the idea that the spherules tend to cluster around carbonate veins (represented by white overlay), but a considerable amount does also appear in regions where no carbonate veins are present. A particle area distribution for the carbonate spherules (Figure 20c) follows a lognormal trend, which indicates that the spherules nucleated at the same time and have experienced the same amount of growth. These results suggest that CO_2-rich fluids entered the rocks through cracks and pre-existing veins, which acted as pathways for the fluid to reach the porous serpentine in order to nucleate carbonates. This represents the onset of carbonation of serpentinite in the process to form listvenite. Fluids migrating through the veins would subsequently travel through pores in the rock and diffuse through the sample, leading to a coupled process of serpentine dissolution and carbonate precipitation.
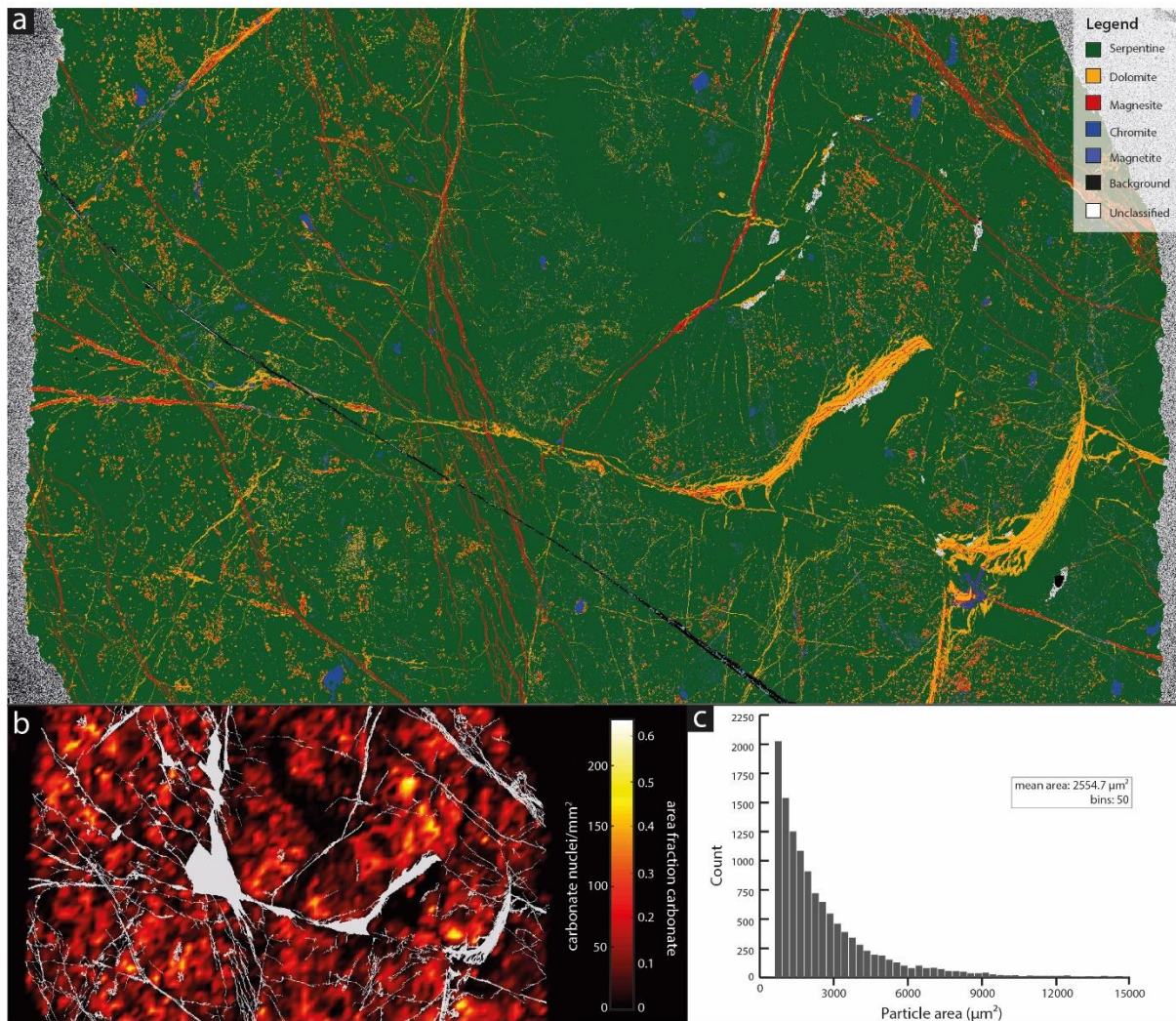
Figure 20 (a) TIMA map of ophicarbonate sample 44-01-08-13, showing all present phases (serpentine, dolomite, magnesite, chromite, magnetite). (b) Particle density map displaying area fraction of carbonate and number of carbonate nuclei per mm^2. White overlay represents the carbonate veins. (c) Particle area distribution for carbonate spherules. The data fits with a lognormal distribution.

5.1.2.2 Growth and evolution of carbonate spherules

The spherulitic grains are a distinct feature in both ophicarbonates and listvenites, making up a large part of the matrix despite their small size (50-100µm). Although they are abundant in the Oman samples, they have not been observed in any of the carbonated ophiolites from Atlin, Canada or Linnajavri, Norway. They do not only appear as single features, but also cluster together and form extensive networks and aggregates. This leads to the idea that several stages in the evolution of carbonate spherule growth can be recognized in the samples. This evolution, for both ophicarbonates and listvenites, is displayed in Figure 21. The spherules firstly appear as separate grains, clearly showing multiple zones, often in a heterogeneous and fine grained matrix. They then start to cluster together, forming large networks of spherules, but their grain boundaries and inner zoning patterns can still be recognized. Subsequently, the clustered carbonates form aggregates, without identifiable grain boundaries but with

27

the inner zoning patterns still visible. These aggregates are the latest detectable stage in the ophicarbonates. In the listvenites, however, separate spherules and aggregates are overgrown by younger, euhedral magnesite. With electron probe microanalysis, the spherulitic grains can still be identified within the euhedral overgrowth due to their different chemical composition (Figure 16).

Similar spherical carbonate grains with chemically zoned successive layers have been identified by Gysi and Stefánsson (2012) during experiments performed at 75°C, although these are much smaller than the carbonate spherules found in the Oman listvenite (5-15 µm). Typical zoning arranged in concentric layers indicates that carbonates were not formed by mineral replacement reactions, but carbonate precipitation is coupled to serpentine dissolution. The spherules observed by Gysi and Stefánsson (2012) are composed of ankerite and have an Fe-rich core, whereas they become increasingly rich in Ca and Mg towards the rims. Gysi and Stefansson (2012) argue that the zonation reflects the effects of the change in chemical composition of the solution on the extent of the reaction. In the case of these ankerite grains, formation of Fe-Mg carbonates was followed by production of more Ca-Mg-rich carbonates. This is explained by the lower hydration energy of Fe^{2+} compared to the hydration energies of Mg^{2+} and Ca^{2+}, leading to slow precipitation rates for Mg and Ca carbonates at low temperature. The spherules in the Oman ophicarbonates show a similar relationship to the ankerite spherules (Fe-rich core, Ca-rich rim). The zoning pattern in these grains could therefore be explained by the low hydration energy of Fe^{2+} compared to Ca^{2+}. However, the conditions of carbonate formation are significantly different for the experiments of Gysi and Stefansson (2012) and the natural system observed in Oman. The experiments described above can be defined as an open system, since the carbonates precipitate directly from solution. In contrast, the carbonates in the samples from Oman are formed in a closed system, because they formed in isolated sites within the serpentine matrix, where fluid access is limited by the diffusion rate. If the fluid is highly saturated in Mg or Fe compared to Ca, magnesite would precipitate, leading to the enrichment of the remaining solution in Ca. Subsequently, dolomite is able to form. If the fluid composition continues to vary in this manner, this might be able to produce the alternating mineralogy that can be observed in the zoned carbonate spherules.
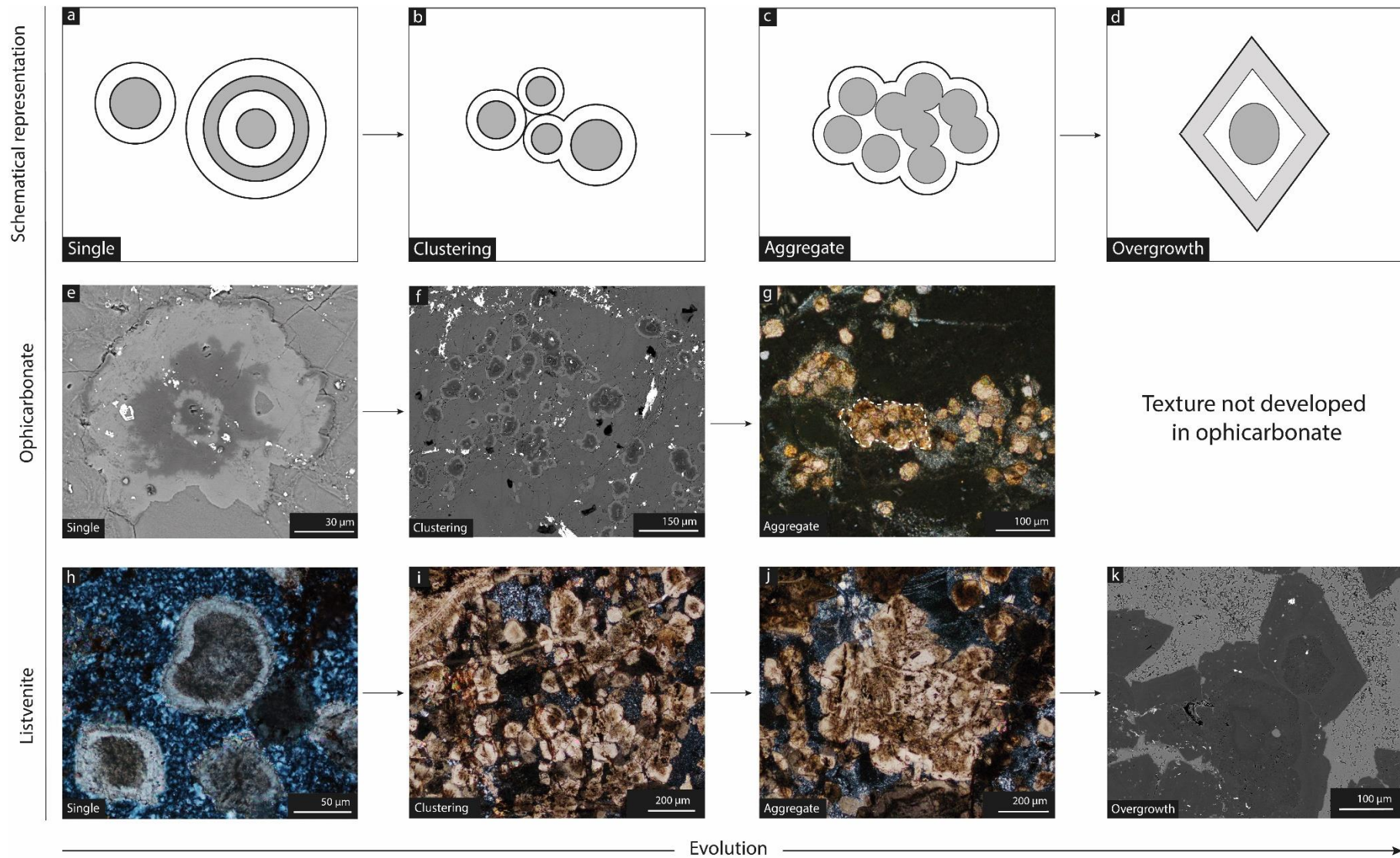
Figure 21 Evolutionary diagram for the carbonate spherules in ophicarbonates and listvenites.

The euhedral magnesite grains in the listvenites (Figure 6b, c and 16) show an oscillatory zoning pattern. Electron microprobe data has shown that this zonation is caused by variations in Fe, Mg and Ca concentrations. Purvis (1989) argues that concentric zoning in magnesite is produced by precipitation from a pore fluid with changing composition, although the reasons for this change are not fully understood. Reeder (1991) agrees with this theory, saying that concentric zoning reflects the changing crystal composition at the growth surface, posing as a method to indicate the changes in fluid properties and environmental conditions during growth. However, besides changes in bulk fluid properties, oscillatory zoning might reflect variations in growth conditions. For example, synthetic calcite showing oscillatory zoning only grows in a system which is far from equilibrium, exposing it to high supersaturation and growth rate (Reeder et al. 1990). Oscillatory zoning in listvenite magnesite could thus either reflect changes in bulk fluid composition, or an instability in the growth process.

Zonation in magnesite due to changes in Fe concentrations has also been documented by Hansen et al. (2005) and (Tominaga et al., 2017). During carbonation of serpentinite, magnetite is destroyed, but mass-balance calculations show that Fe is preserved within magnesite (Hansen et al., 2005). This is supported by magnetic field data from Tominaga et al. (2017). A decreasing magnetic field intensity across a soapstone – listvenite interface and observed magnetite breakdown in listvenite indicates that non-magnetic minerals are forming at the expense of magnetite during the formation of listvenite. This would indicate that the Fe component in zoned magnesite crystals are produced from the breakdown of magnetite and other oxides such as chromite during carbonation of serpentinite.

5.1.2.3 Spherulite growth in porous media
Spherulites are formed in solids under high non-equilibrium conditions (Magill, 2001). It is generally assumed that high viscosity or presence of heterogeneities (such as impurities or molecular defects) are required to form these textures (Gránásy et al., 2005; Beck and Andreassen, 2010). Experiments on spherulitic growth of calcium carbonate (vaterite) indicate that increased levels of supersaturation produce fully grown spherulites (Andreassen et al., 2010). This is supported by predictions by Sunagawa (2005), who argues that the crystal morphology is dependent on the driving force (or supersaturation) for crystallization (Figure 22). As the driving force is increased, the shape of a crystal will evolve from monocrystalline to hopper type, to dendritic and eventually to spherulitic due to radiating growth. In conclusion, in order to nucleate spherulitic particles, the supersaturation must be of high enough values.
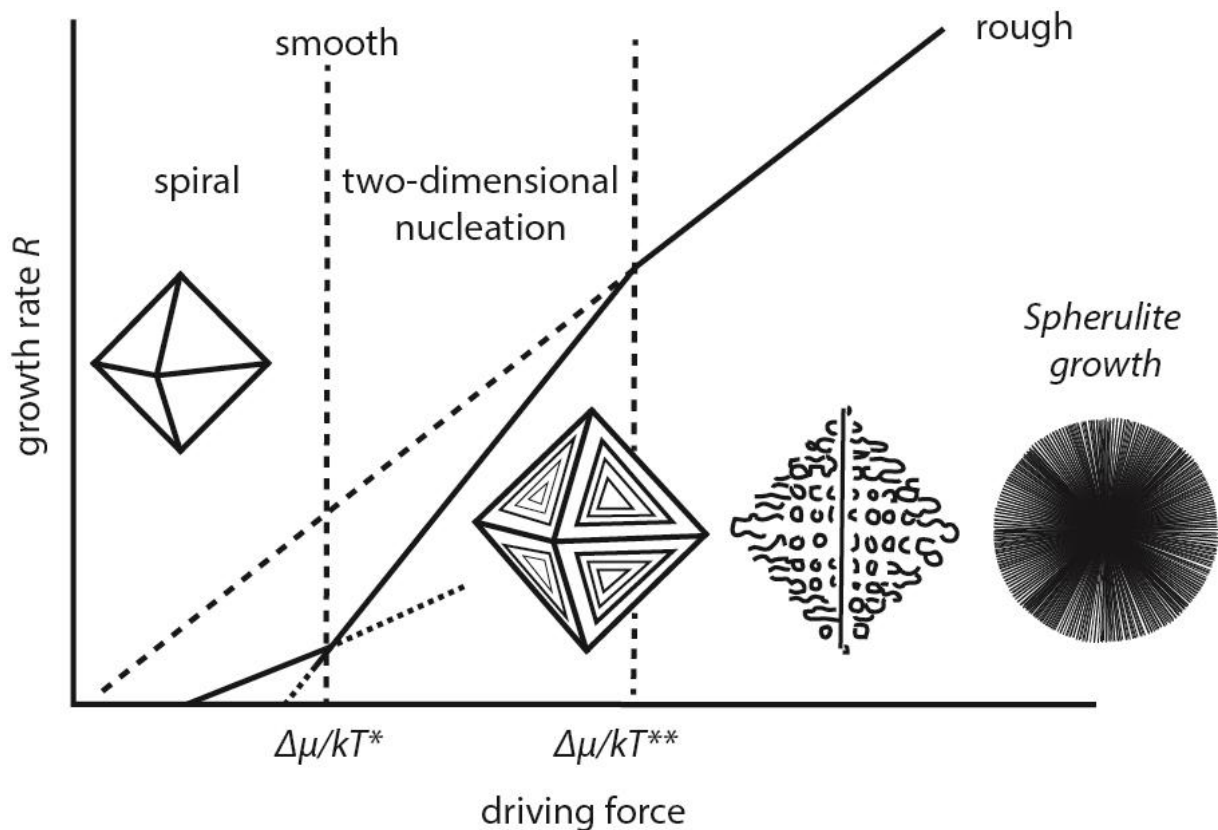
Figure 22 Evolution of crystal morphology with changing driving force (supersaturation), modified after Sunagawa (2005). Spherulites were formed due to radiating growth as indicated in the graph, when the driving force has been increased sufficiently.

The porosity in serpentinite, the earliest host rock of the carbonate grains, was found to be distinct compared to the homogeneous carbonate in the spherules (Figure 12). According to Prieto et al. (1990) and Putnis et al. (1995), a certain threshold supersaturation must be achieved in order to nucleate materials in a porous media. Therefore, the supersaturation of Mg, Ca and Fe must have been sufficient enough to nucleate particles in the porous host rock, and to eventually produce spherical carbonates. Prieto (2014) argues that the induction time (the time between initiation of supersaturation and the first sign of nucleation) depends on the solution volume. In fine porous media, where transport occurs via diffusion, the volume of a single pore is considered to be the solution volume. The smaller the solution volume, or pore volume, the longer the induction time. Nucleation in small pores will thus only be favourable when the supersaturation is increased considerably, leading to extremely high supersaturation values and conditions far from equilibrium. In the case of the carbonated serpentinites from Oman, this leads to the production of disequilibrium features such as spherulites. Over time, the supersaturation decreases, leading to equilibrium conditions and the production of euhedral carbonate (Figure 22).

5.1.2.4 Growth mechanism

The texture and development of the carbonate spherules in ophicarbonates and listvenites are very similar to each other. It can therefore be argued that these rocks represent different stages in the evolution of the spherulites, from single spherule formation in ophicarbonates to clustering in listvenites. However, there are several indications that this theory does not accurately describe the development of the carbonate spherules. The most striking property of the listvenite spherules is that their rim is composed of Ca-rich magnesite instead of dolomite, as identified in the ophicarbonate spherules. Electron probe microanalysis shows that the CaO concentration in the rim of listvenite spherules is 0.87 wt%, compared to 17.53 wt% in ophicarbonate spherules. If the ophicarbonate spherules would directly evolve into listvenite spherules, a considerable amount of Ca would need to be removed, and the crystal structure of dolomite would be altered into that of magnesite. Even though there is a significant amount of dolomite in the listvenites that might account for the uptake of Ca, this would not explain the sudden change in crystal structure.

An alternative explanation for the variation in Ca would be that the ophicarbonates and listvenites were exposed to different environmental conditions. Since the listvenites have been more pervasively carbonated than the ophicarbonates, this could suggest that the permeability and amount of fluid influx were much greater in the precursor rock of the listvenites, due to a higher amount of fractures, cracks and veins. In the ophicarbonates, the CO_2 in the fluid would be consumed more rapidly than in the listvenites, causing the activity of Ca to increase considerably due to the production of magnesite. The rims of the ophicarbonate spherules thus represent the last stage of fluid precipitation, reflecting the high Ca activity in the fluid. The listvenites, on the other hand, did not run out of CO_2-rich fluid at that same time, and the activity of Ca in the bulk fluid would be lower. The rims of the listvenite spherules thus reflect the lower activity of Ca in the fluid that migrated through these rocks. In conclusion, the starting point of nucleation for the carbonate spherules would be the same for the ophicarbonates and listvenites, but the reaction progress varies due to different fluid compositions.

5.2 Alteration scenarios

5.2.1 Alteration sequence

The bulk rock composition of the ophicarbonates and listvenites with depth shows that carbonation was isochemical, with the exception of volatiles (H_2O and CO_2). The SiO_2/MgO ratio remains constant throughout the altered ophiolite, indicating that SiO_2 was not added to the system. However, listvenites were produced in a system that was initially undersaturated in quartz. The production of quartz is solely dependent on the introduction of CO_2, due to the increase in SiO_2 activity during the formation of magnesite (Klein and Garrido, 2011).

Addition of H_2O and CO_2 to the system was responsible for serpentinization and carbonation of ultramafic rocks. However, it is not known exactly how the fluids interacted with these rocks. The following scenarios can be used to describe the alteration of the Oman ophiolite sequence:

1. The influx of CO_2-rich fluid leads to coupled progressive serpentinization and the formation of ophicarbonate and listvenite. As olivine reacts with H_2O, the concentration of CO_2 in the fluid increases and results in the production of magnesite and dolomite. The initiation of carbonation is observed as the nucleation of carbonate spherules. This scenario could explain the even distribution of carbonate spherules across the samples, since the concentration of CO_2 is constant through the whole sample. However, it would be difficult to explain how this fluid could lead to extensive listvenite formation, since it is not likely that the concentration of CO_2 is sufficient enough to produce such significant amounts of carbonate. The increasing concentration of CO_2 in the fluid could be responsible for the nucleation of carbonate spherules, but would quickly diminish to very low levels if there is no continuous influx of CO_2-rich fluid. Furthermore, listvenites appear to form locally in the presence of fractures, leading to high permeability. If serpentinization and carbonation would be coupled, the CO_2 concentration would be constant throughout the rocks and listvenites would be evenly distributed.

2. The influx of fluids leads to serpentinization of peridotites decoupled from carbonation process. A second pulse of fluids with a high concentration of CO_2 follows, which leads to the formation of ophicarbonates and listvenites. Ophicarbonates are produced in places with a low permeability, whereas listvenites are produced at sites of elevated structural permeability. This would explain the presence of both ophicarbonates and listvenites in the ophiolite, which has been caused by the amount of CO_2 that was able to reach and alter the serpentinite.

The textures in the ophicarbonates and listvenites provide more information about the fluid properties. At the start of alteration, large amounts of H_2O will have reacted with ultramafic rocks to form serpentinite and serpentine veins. Subsequently, CO_2-rich fluids caused the onset of carbonation and produced the earliest carbonate spherules and magnesite veins. Breakdown of magnetite, chromite and other oxides, associated with formation of listvenite, would provide Fe for Fe-rich carbonate veins, spherules and matrix serpentine. Continued carbonation led to the production of quartz in veins and within the listvenite matrix. During the last stage of carbonation, fluids became more enriched in Ca and precipitated dolomite veins and the outer rims of the carbonate spherules. Although the concentration of Ca increased during this stage, calcite was never observed in these samples.

5.2.2 Absence of talc

The most striking difference between the samples investigated in this study and listvenites at other locations is the absence of talc in the rocks. Talc has been observed in other parts of the Oman ophiolite by Falk and Kelemen (2015), in Atlin, Canada, by Hansen et al. (2005) and in extremely large proportions in soapstone at Linnajavri, Norway, by Beinlich et al. (2012). In these cases, carbonation of serpentinite would lead to the production of talc, magnesite and water (Hansen et al., 2005). Talc then reacts with CO_2 to form the typical listvenite assemblage of magnesite and quartz (Hansen et al., 2005; Kelemen et al., 2011). According to thermodynamic predictions at 100 bar and a temperature range of 20-150°C, talc should be present in the system (Figure 23). Since it was not recognized in the samples used for this study, it can be concluded that the formation of talc in this environment is restricted by reaction kinetics. In addition, the Oman samples contain abundant textural evidence for disequilibrium alteration, such as spherulitic carbonates, implying that an equilibrium thermodynamic model is not suitable to describe these rocks.
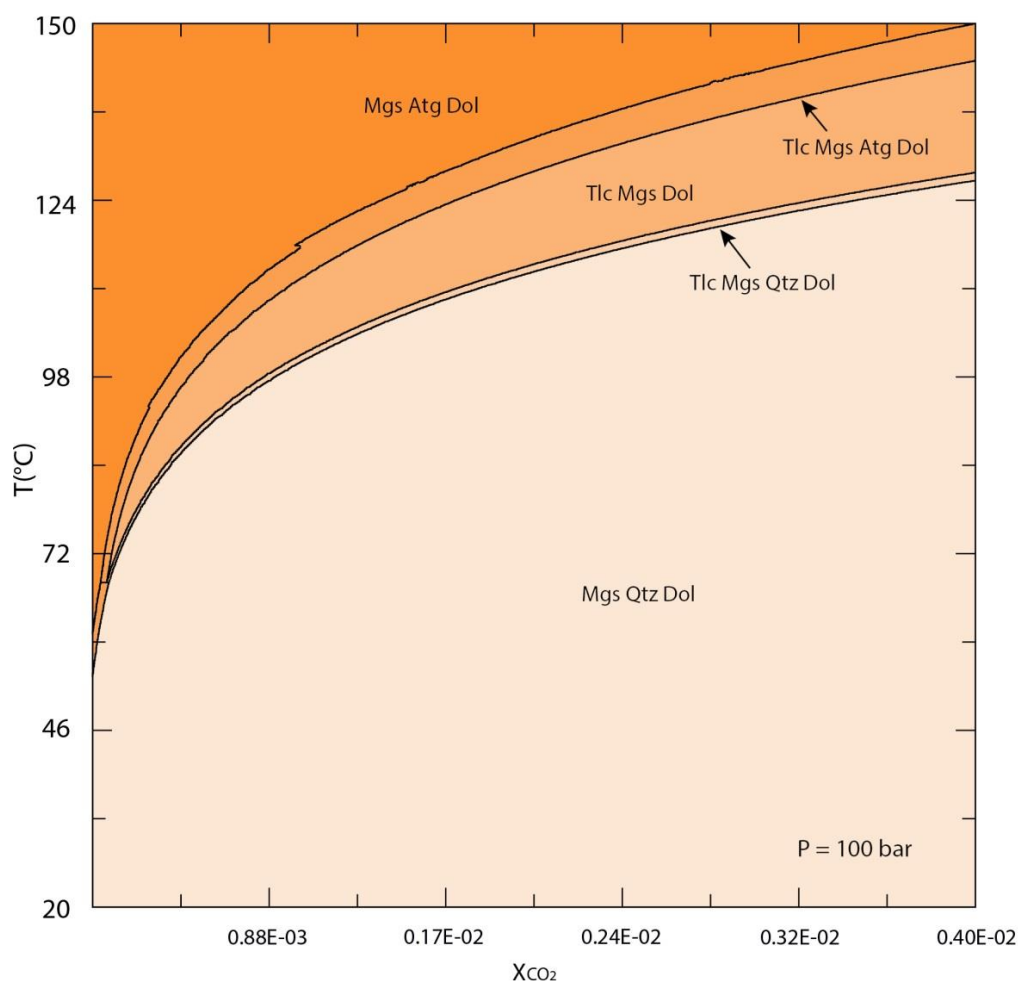

Figure 23 Isobaric $T - X_{CO_2}$ diagram constructed with PerpleX (Connolly, 1990) at P = 100 bar, showing equilibria in a system with magnesite (Mgs), antigorite (Atg), dolomite (Dol), talc (Tlc) and quartz (Qtz).

Aside from kinetic restrictions, talc may never have formed in this part of the ophiolite due to structural controls, such as on Tinos, Cyclades, Greece (Hinsken et al., 2017). Hinsken et al. argue that it is likely for talc to not have formed at all, since serpentinite carbonation is related to structurally-controlled fluid influx, in contrast to the massive carbonation front that is observed in Linnajavri, Norway (Beinlich et al., 2012). The same applies for the listvenites in the Oman ophiolite, which are associated with extensive fracturing and veining, thus allowing the infiltration of significant amounts of fluid enriched in CO_2. The high level of permeability will permit direct carbonation of serpentinite leading to the production of magnesite and quartz, instead of forming a reaction front associated with the production of talc.

6. Conclusions & implications

The microstructures in the ophicarbonates and listvenites of the Oman ophiolite indicate pervasive carbonation of ultramafic rocks. Although it has been argued in several studies (Kelemen and Matter, 2008; Kelemen et al., 2011; Falk and Kelemen, 2015) that the carbonated rocks were formed due to carbonation of peridotites, no evidence was found for alteration of olivine. The absence of olivine relicts and the presence of serpentine inclusions in carbonate spherules lead to the conclusion that the ophicarbonates and listvenites from Oman were formed by carbonation of serpentinite. This implies that carbonation of the Semail ophiolite was either coupled with serpentinization of peridotites, or occurred after complete serpentinization.

Extensive veining reflects the presence of pathways such as fractures for CO_2-rich fluids that lead to listvenite formation. The earliest veins that can be recognized in the rocks are serpentine veins, followed by magnesite, quartz and dolomite veins, suggesting that fluids of different composition have affected the rocks over time. Distinctive carbonate spherules, composed of a magnesite core and a dolomite (in ophicarbonates) or Ca-rich magnesite (in listvenites) rim, represent the onset of carbonation in these samples and evolve with time from separate grains to clusters that are eventually overgrown by euhedral carbonate in the most pervasively altered listvenite samples. The carbonate spherules are all the same size and seem to be concentrated around carbonate veins, which indicates that they were produced by the same event and experienced the same amount of growth. Separate carbonate spherules further away from the veins were formed due to fluid diffusion through the porous serpentine matrix. The CO_2-rich fluid that was responsible for the production of multiple vein generations and carbonate spherules changed in composition over time. Early fluid-rock interactions will have produced the first magnesite veins and carbonate spherules. The breakdown of magnetite, chromite and other oxides provided enough iron for the zonation in Fe-rich serpentine, carbonate spherules, magnesite grains and veins. Due to continued carbonation, significant amounts of quartz were produced in veins and matrix material. Finally, the fluids became enriched in Ca, leading to the production of coarse grained dolomite veins and an outer Ca-rich rim in the carbonate spherules. The absence of talc in the Oman

ophicarbonates and listvenites can be explained by restrictive kinetic effects and structurally controlled fluid flow, leading to direct production of magnesite and quartz. Textural observations suggest that pervasive carbonation was dependent on deformation of the ophiolite, such as extensive fracturing, and the pulsed supply of considerable amounts of fluid available during ophiolite obduction. This implies that fluid influx and carbonation of ultramafic rocks is substantial in the forearcs of subduction zones.

7. Acknowledgements

8. References

Allemann F. (1972) The ophiolite radiolarite belt of the North Oman mountains. *Eclogae Geol. Helv.* **65**, 657–697.

Andreassen J. P., Flaten E. M., Beck R. and Lewis A. E. (2010) Investigations of spherulitic growth in industrial crystallization. *Chem. Eng. Res. Des.* **88**, 1163–1168. Available at: http://dx.doi.org/10.1016/j.cherd.2010.01.024.

Armstrong J. T. (1988) Quantitative analysis of silicates and oxide minerals: Comparison of Monte-Carlo, ZAF and Phi-Rho-Z procedures. *Microbeam Anal.*, 239–246.

Beck R. and Andreassen J. P. (2010) Spherulitic growth of calcium carbonate. *Cryst. Growth Des.* **10**, 2934–2947.

Beinlich A., Plümper O., Hövelmann J., Austrheim H. and Jamtveit B. (2012) Massive serpentinite carbonation at Linnajavri , N – Norway. *Terra Nov.* **24**, 446–455.

Bons P. D., Elburg M. A. and Gomez-Rivas E. (2012) A review of the formation of tectonic veins and their microstructures. *J. Struct. Geol.* **43**, 33–62. Available at: http://dx.doi.org/10.1016/j.jsg.2012.07.005.

Coleman R. G. (1981) Tectonic setting for ophiolite obduction in Oman. *J. Geophys. Res.* **86**, 2497–2508.

Connolly J. A. D. (1990) Multivariable phase diagrams: An algorithm based on generalized thermodynamics. *Am. J. Sci.* **290**, 666–718.

Dasgupta R. and Hirschmann M. M. (2010) The deep carbon cycle and melting in Earth's interior. *Earth Planet. Sci. Lett.* **298**, 1–13.

Donovan J. J., Snyder D. A. and Rivers M. L. (1993) An improved interference correction for trace element analysis. *Microbeam Anal.* **2**, 23–28.

Donovan J. J. and Tingle T. N. (1995) An improved mean atomic number background correction for quantitative microanalysis. *Microbeam Anal.*, 209–210.

Emam A. and Zoheir B. (2013) Au and Cr mobilization through metasomatism: Microchemical evidence from ore-bearing listvenite, South Eastern Desert of Egypt. *J. Geochemical Explor.* **125**, 34–45. Available at: http://dx.doi.org/10.1016/j.gexplo.2012.11.004.

Falk E. S. (2014) Carbonation of Peridotite in The Oman Ophiolite. .

Falk E. S. and Kelemen P. B. (2015) Geochemistry and petrology of listvenite in the Samail ophiolite , Sultanate of Oman: Complete carbonation of peridotite during ophiolite emplacement. *Geochim. Cosmochim. Acta* **160**, 70–90. Available at: http://dx.doi.org/10.1016/j.gca.2015.03.014.

Gerdemann S. J., O'Connor W. K., Dahlin D. C., Penner L. R. and Rush H. (2007) Ex situ aqueous mineral carbonation. *Environ. Sci. Technol.* **41**, 2587–2593.

Glennie K. W., Boeuf M. G. A., Hughes Clarke M. W., Moody-Stuart M., Pilaar W. and Reinhardt B. M. (1974) Geology of the Oman Mountains. *Verh. van het K. Ned. Geol. Mijnbouwkd. Genoot.* **31**, 423.

Gorman P. J., Kerrick D. M. and Connolly J. A. D. (2006) Modeling open system metamorphic decarbonation of subducting slabs. *Geochemistry, Geophys. Geosystems* **7**.

Gránásy L., Pusztai T., Tegze G., Warren J. A. and Douglas J. F. (2005) Growth and form of spherulites. *Phys. Rev. E* **72**, 1–15.

Gysi A. P. and Stefánsson A. (2012) Mineralogical aspects of CO2 sequestration during hydrothermal basalt alteration - An experimental study at 75 to 250°C and elevated pCO2. *Chem. Geol.* **306**–**307**, 146–159. Available at: http://dx.doi.org/10.1016/j.chemgeo.2012.03.006.

Hacker B. R. and Gnos E. (1997) The conundrum of samail: explaining the metamorphic history. *Tectonophysics* **279**, 215–226.

Halls C. and Zhao R. (1995) Listvenite and related rocks: perspectives on terminology and mineralogy with reference to an occurrence at Cregganbaun, Co. Mayo, Republic of Ireland. *Miner. Depos.* **30**, 303–313.

Hansen L. D., Dipple G. M., Gordon T. M. and Kellett D. A. (2005) Carbonated serpentinite (listwanite) at Atlin, British Columbia: A geological analogue to carbon dioxide sequestration. *Can. Mineral.* **43**, 225–239.

Hinsken T., Bröcker M., Strauss H. and Bulle F. (2017) Geochemical, isotopic and geochronological characterization of listvenite from the Upper Unit on Tinos, Cyclades, Greece. *Lithos* **282**–**283**, 281–297. Available at: http://dx.doi.org/10.1016/j.lithos.2017.02.019.

Kelemen P. (2014) ICDP Oman Drilling appendices.

Kelemen P. (2014) ICDP Oman Drilling Proposal.

Kelemen P. B. and Manning C. E. (2015) Reevaluating carbon fluxes in subduction zones, what goes

down, mostly comes up. *Proc. Natl. Acad. Sci.* **112**, E3997–E4006.

Kelemen P. B. and Matter J. (2008) In situ carbonation of peridotite for CO2 storage. *Proc. Natl. Acad. Sci.* **105**, 17295–17300.

Kelemen P. B., Matter J., Streit E. E., Rudge J. F., Curry W. B. and Blusztajn J. (2011) Rates and Mechanisms of Mineral Carbonation in Peridotite: Natural Processes and Recipes for Enhanced, in situ CO2 Capture and Storage. *Annu. Rev. Earth Planet. Sci.* **39**, 545–576.

Kelemen, P., Matter, J., Teagle, D.A.H., Coggon, J.A., Harris, M., Takazawa, E., Michibayashi, K., de Obeso, J.-C., and the Oman Drilling Project Phase 1 Science Team (2019 - in prep). Proceedings of the Oman Drilling Project: Initial Results Phase 1. Texas A&M University (College Station, TX).

Klein F. and Garrido C. J. (2011) Thermodynamic constraints on mineral carbonation of serpentinized peridotite. *Lithos* **126**, 147–160. Available at: http://dx.doi.org/10.1016/j.lithos.2011.07.020.

Lanphere M. A. (1981) K-Ar ages of metamorphic rocks at the base of the Samail Ophiolite, Oman. *J. Geophys. Res. Solid Earth* **86**, 2777–2782.

Magill J. H. (2001) Review Spherulites: A personal perspective. *J. Mater. Sci.* **36**, 3143–3164.

Matter J. M. and Kelemen P. B. (2009) Permanent storage of carbon dioxide in geological reservoirs by mineral carbonation. *Nat. Geosci.* **2**, 837–841. Available at: http://dx.doi.org/10.1038/ngeo683.

Nasir S., Al Sayigh A. R., Al Harthy A., Al-Khirbash S., Al-Jaaidi O., Musllam A., Al-Mishwat A. and Al-Bu'saidi S. (2007) Mineralogical and geochemical characterization of listwaenite from the Semail ophiolite, Oman. *Chemie der Erde-Geochemistry* **67**, 213–228.

Paukert A. N., Matter J. M., Kelemen P. B., Shock E. L. and Havig J. R. (2012) Reaction path modeling of enhanced in situ CO2 mineralization for carbon sequestration in the peridotite of the Samail Ophiolite, Sultanate of Oman. *Chem. Geol.* **330–331**, 86–100. Available at: http://dx.doi.org/10.1016/j.chemgeo.2012.08.013.

Prieto M. (2014) Nucleation and supersaturation in porous media (revisited). *Mineral. Mag.* **78**, 1437–1447. Available at: http://openurl.ingenta.com/content/xref?genre=article&issn=0026-461X&volume=78&issue=6&spage=1437.

Prieto M., Putnis A. and Fernandez-Diaz L. (1990) Factors controlling the kinetics of crystallization: Supersaturation evolution in a porous medium. Application to barite crystallization. *Geol. Mag.* **127**, 485–495.

Purvis K. (1989) Zoned authigenic magnesites in the Rotliegend Lower Permian, southern North Sea. *Sediment. Geol.* **65**, 307–318.

Putnis A., Prieto M. and Fernandez-Diaz L. (1995) Fluid supersaturation and crystallization in porous media. *Geol. Mag.* **132**, 1–13.

Reeder R. J. (1991) An overview of zoning in carbonate minerals. *Lumin. Microsc. Spectrosc. Qual. Quant. Appl.*, 77–82.

Reeder R. J., Fagioli R. O. and Meyers W. J. (1990) Oscillatory zoning of Mn in solution-grown calcite crystals. *Earth Sci. Rev.* **29**, 39–46.

Rioux M., Bowring S., Kelemen P., Gordon S., Miller R. and Dudás F. (2013) Tectonic development of the Samail ophiolite: High-precision U-Pb zircon geochronology and Sm-Nd isotopic constraints on crustal growth and emplacement. *J. Geophys. Res.* **118**, 2085–2101.

Rose G. (1837) Mineralogisch-geognostische Reise nach dem Ural, dem Altai und dem Kaspischen Meere, Band I. *Reise nach dem noerdlichen Ural und dem Altai. Berlin, CW Eichoff (Verlag der Sanderschen Buchhandl.)* **I–VII**.

Searle M. P. and Malpas J. (1980) Structure and metamorphism of rocks beneath the Semail ophiolite of Oman and their significance in ophiolite obduction. *Earth Environ. Sci. Trans. R. Soc. Edinburgh* **71**, 247–262.

Searle M. P., Waters D. J., Garber J. M., Rioux M., Cherry A. G. and Ambrose T. K. (2015) Structure and metamorphism beneath the obducting Oman ophiolite: Evidence from the Bani Hamid granulite , northern Oman mountains. *Geosphere* **11**, 1812–1836.

Stanger G. (1985) Silicified serpentinite in the Semail nappe of Oman. **18**, 13–22.

Streit E., Kelemen P. and Eiler J. (2012) Coexisting serpentine and quartz from carbonate-bearing serpentinized peridotite in the Samail Ophiolite, Oman. *Contrib. to Mineral. Petrol.* **164**, 821–837.

Sunagawa I. (2005) Driving force and morphology of crystals. In *Crystals: Growth, Morphology, & Perfection* pp. 51–52.

Tominaga M., Beinlich A., Lima E. A., Tivey M. A., Hampton B. A., Weiss B. and Harigane Y. (2017) Multi-scale magnetic mapping of serpentinite carbonation. *Nat. Commun.* **8**, 1–10. Available at: http://dx.doi.org/10.1038/s41467-017-01610-4.

Appendices

Figure A1 (a) plane polarized and (b) cross polarized overview scan of sample 13-02-73-77, listvenite containing magnesite, dolomite, quartz, oxides and minor hematite and chromite.
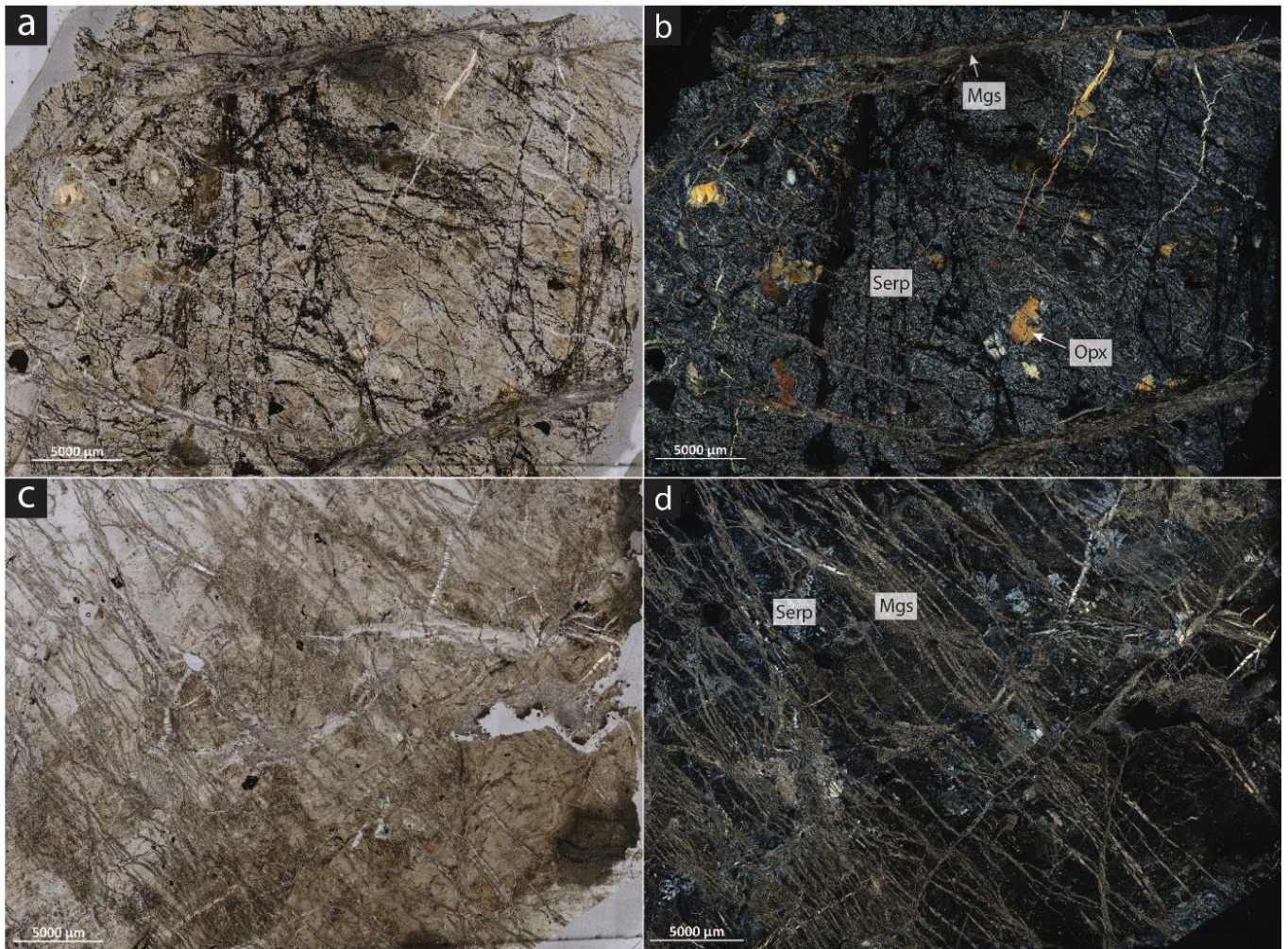
Figure A2 (a) plane polarized and (b) cross polarized overview scan of sample 39-04-68-72, serpentinite containing serpentine, magnesite, oxides, Cr-spinel and relicts of orthopyroxene. (c) plane polarized and (b) cross polarized overview scan of sample 44-03-60-63, ophicarbonate containing serpentine, magnesite, dolomite and oxides.
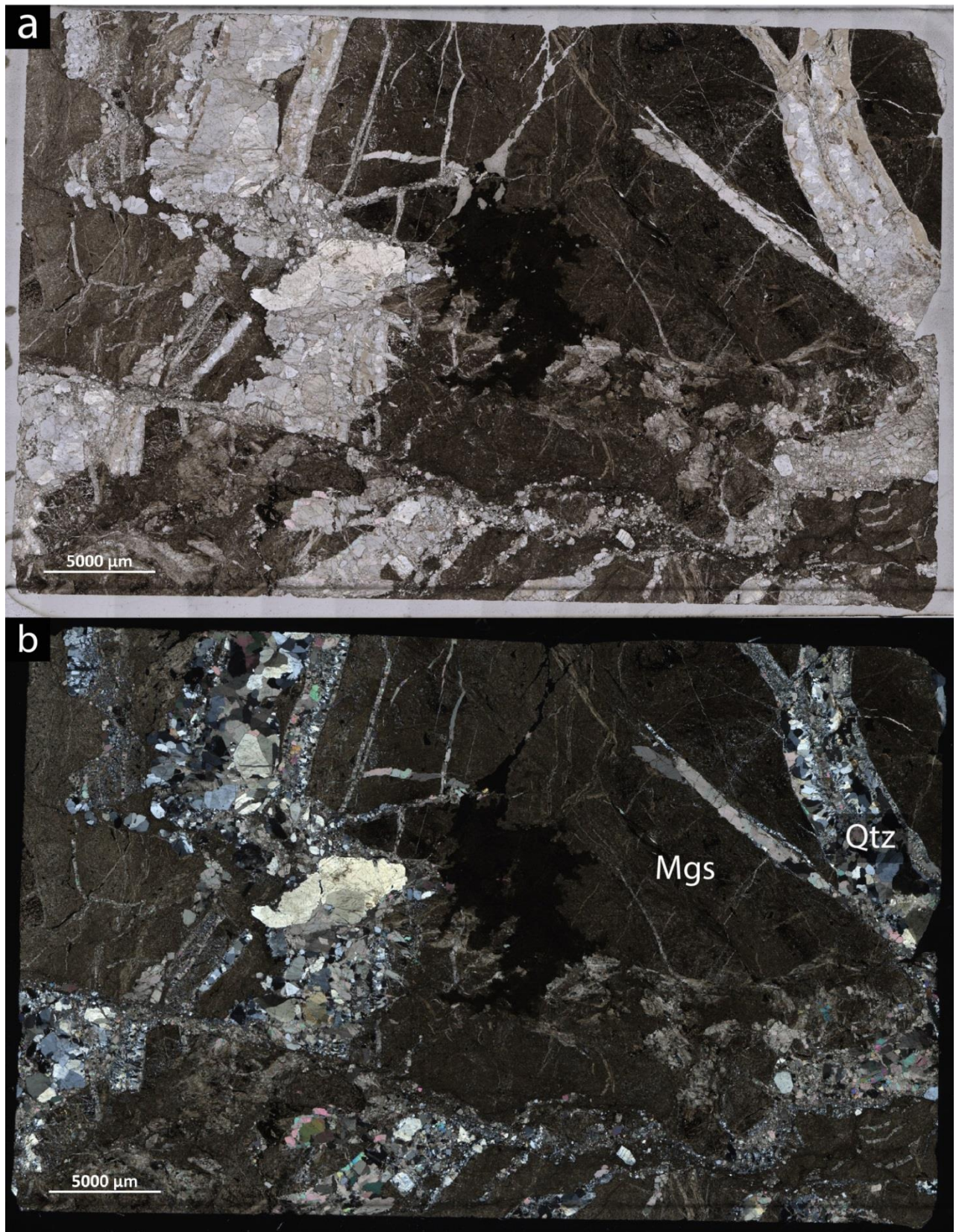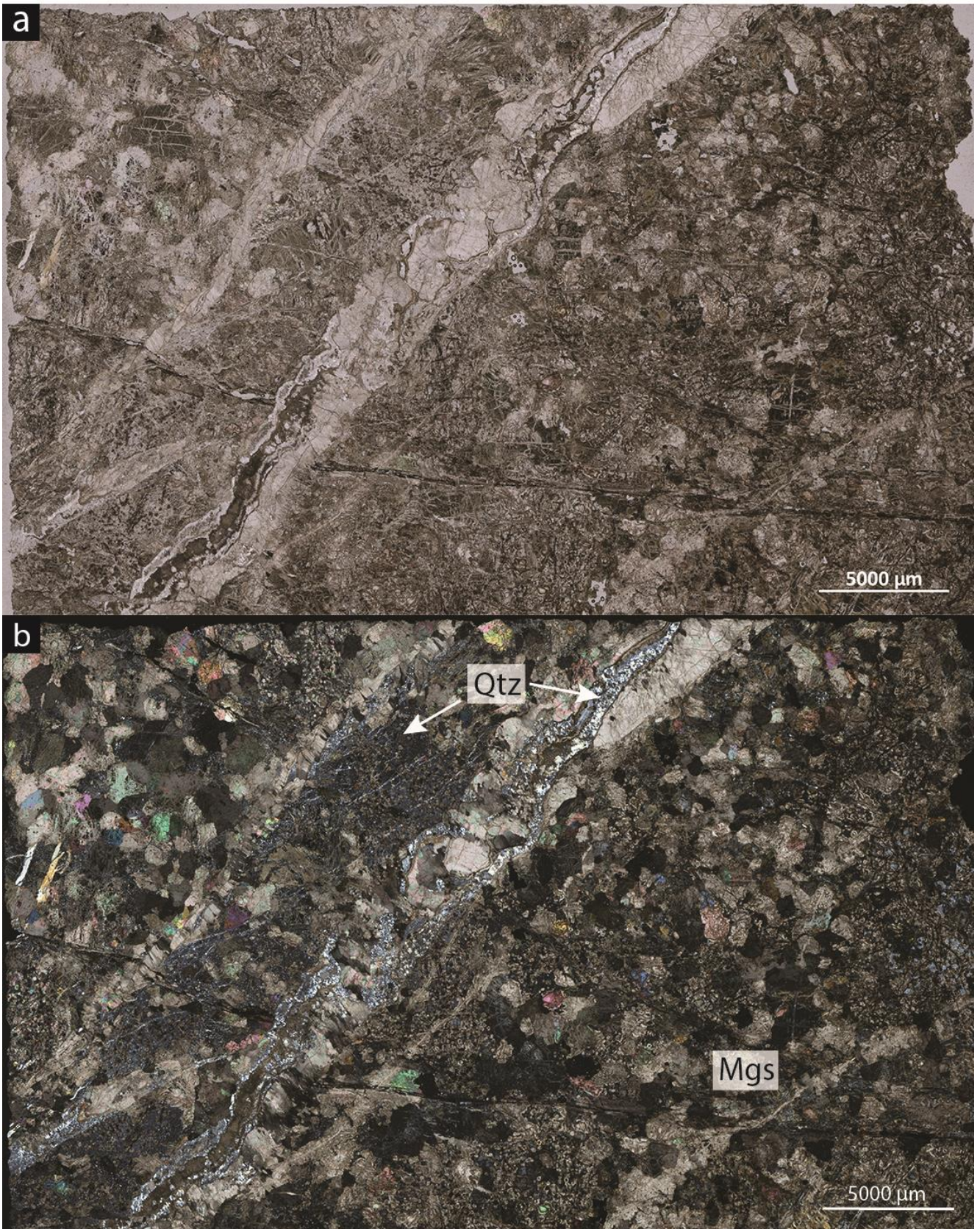
Figure A3 (a) plane polarized and (b) cross polarized overview scan of sample 60-03-29-33, listvenites containing magnesite, dolomite, quartz, fuchsite and oxides.

Core	Section	Top depth (cm)	Bottom depth (cm)	Type	Top depth (m)	Mgs	Dol	Qtz	Serp	Fuch	Spl	Opx	Mag	Hem	Chr
13	02	73	77	listvenite	21.89	x	x	x					x	x	x
32	02	22	26	listvenite	67.45	x	x	x					x	x	x
39	04	68	72	serpentinite	84.27	x			x		x	x	x		x
40	02	62	66	ophicarbonate	85.91	x			x			x	x		
41	04	25	29	ophicarbonate	90.11	x			x			x	x		x
43	02	10	15	ophicarbonate	94.89	x	x		x		x		x		
44	01	8	13	ophicarbonate	97.15	x			x			x	x		x
44	03	60	63	ophicarbonate	98.71	x			x				x		x
52	01	41	46	listvenite	118.5	x	x	x		x			x		
60	03	29	33	listvenite	141.3	x	x	x		x			x		
65	01	5	9	listvenite	155.1	x	x	x		x	x		x		
67	04	69	73	listvenite	163.26	x	x	x		x	x		x		x
68	02	14	18	listvenite	165.05	x	x	x		x	x		x		
72	04	39	43	listvenite	178.74	x	x	x					x		
77	03	11	15	listvenite	193.23	x	x	x					x		

Table S1 Mineral assemblage in samples taken from the Oman ophiolite during the Oman drilling project.

Table S2 Representative electron probe microanalysis of carbonates within carbonates and listvenites

Sample ID	BT1B_44-01	BT1B_44-01	BT1B_44-03	BT1B_44-03	BT1B_44-03	BT1B_44-03	BT1B_60-03	BT1B_60-03	BT1B_60-03	BT1B_60-03	BT1B_60-03	BT1B_60-03	BT1B_65-01	BT1B_65-01	BT1B_65-01	BT1B_68-02	BT1B_68-02	BT1B_72-04	BT1B_72-04
Mineralogy	Magnesite	Dolomite	Fe-rich magnesite	Magnesite	Dolomite	Magnesite	Magnesite	Magnesite	Magnesite	Magnesite	Magnesite	Magnesite	Magnesite	Magnesite	Dolomite	Fe-rich magnesite	Magnesite	Dolomite	Magnesite
Texture context	Spherule	Spherule	Vein	Vein	Vein	Branches	Matrix	Matrix	Vein	Vein	Spherule	Spherule	Vein	Vein	Matrix	Vein	Vein	Vein	Vein
Grain context	Core	Rim	Core	Rim			Core	Rim	Core	Rim	Core	Rim	Core	Rim		Core	Rim		
n[1]	1	1	11	16	6	6	2	5	1	2	2	2	4	3	3	1	3	4	7
wt%																			
FeO	5.45	2.88	22.46	9.20	3.72	1.78	5.55	4.74	5.57	6.85	4.09	6.25	8.22	4.27	3.91	20.48	7.33	2.90	9.72
MnO	0.41	0.43	0.06	0.12	0.04	1.45	0.09	0.03	0.10	0.10	0.03	0.03	0.36	0.03	0.15	0.13	0.16	0.10	0.10
MgO	41.52	25.16	28.15	36.31	23.44	43.98	42.80	42.56	42.15	41.52	43.12	39.66	40.38	41.71	18.85	13.32	40.49	19.35	38.06
CaO	0.62	17.53	0.61	0.35	19.31	0.17	0.19	0.27	1.18	0.22	0.23	0.87	0.28	0.51	26.71	0.56	0.36	26.96	0.30
CO_2[2]	50.73	49.37	47.07	50.57	48.93	51.48	50.72	51.10	50.57	50.46	51.23	50.78	50.10	51.26	47.63	50.31	50.45	47.86	49.96
ppm																			
Sr	bdl	468	481	303	2801	340	bdl	457	bdl	bdl	bdl	bdl	bdl	419	bdl	bdl	278	571	bdl
Pr	bdl	bdl	950	950	607	bdl	1503	bdl	762	bdl	661	bdl	bdl	390	bdl	bdl	bdl	588	609
Sm	395	bdl	bdl	300	400	366	bdl	316	bdl	335	410	bdl	392	367	bdl	301	346	298	277
Gd	807	bdl	488	591	481	645	542	683	522	585	bdl	490	517	850	bdl	bdl	bdl	bdl	483
Yb	bdl	1823	bdl	622	1241	bdl	bdl	1020	bdl	718	917	2176	671	2324	bdl	bdl	1051	bdl	1411
Total wt%	99.13	95.90	98.47	96.79	96.06	99.08	99.74	98.99	99.87	99.51	99.04	98.07	99.60	98.26	97.42	84.89	99.04	97.35	98.54
Fe	0.07	0.04	0.31	0.12	0.05	0.02	0.07	0.06	0.07	0.08	0.05	0.08	0.10	0.05	0.05	0.45	0.09	0.04	0.12
Mn	0.01	0.01	0.00	0.00	0.00	0.02	0.00	0.00	0.00	0.00	0.00	0.00	0.00	0.00	0.00	0.00	0.00	0.00	0.00
Mg	0.92	0.64	0.68	0.87	0.59	0.96	0.93	0.94	0.91	0.91	0.95	0.90	0.89	0.94	0.47	0.53	0.90	0.48	0.87
Ca	0.01	0.32	0.01	0.01	0.35	0.00	0.00	0.00	0.02	0.00	0.00	0.01	0.00	0.01	0.48	0.02	0.01	0.48	0.00
Cations p.f.u.[3]	1.00	1.00	1.00	1.00	1.00	1.00	1.00	1.00	1.00	1.00	1.00	1.00	1.00	1.00	1.00	1.00	1.00	1.00	1.00
Oxygen p.f.u.	3	3	3	3	3	3	3	3	3	3	3	3	3	3	3	3	3	3	3

bdl = below detection limit

[1] Number of analyses

[2] Determined stoichiometrically

[3] per formula unit

Table S3 Representative electron probe microanalysis of silicates within ophicarbonates and listvenites

Sample ID	BT1B_44-01	BT1B_44-01	BT1B_44-01	BT1B_44-03	BT1B_44-03	BT1B_44-03	BT1B_65-01	BT1B_65-01
Mineralogy	Serpentine	Serpentine	Bastite	Serpentine	Serpentine	Serpentine	Quartz	Fuchsite
Texture context	Matrix	Vein	Relict	Vein	Sheared matrix	Matrix	Vein	
n[1]	5	2	9	3	3	2	3	5
wt%								
CaO	0.06	0.03	0.15	0.06	0.07	0.16	0.02	0.38
SiO_2	44.29	44.88	43.52	44.83	44.99	44.52	102.11	51.90
MgO	39.97	41.27	36.15	38.24	37.98	36.54	0.03	1.65
Al_2O_3	0.13	0.23	0.89	0.27	0.29	0.72	0.47	24.64
MnO	0.09	bdl	0.08	0.07	0.06	0.08	bdl	0.13
Na_2O	0.02	bdl	0.02	0.02	0.02	0.03	0.02	0.06
TiO_2	0.07	bdl	0.17	0.12	0.14	0.08	bdl	0.08
K_2O	bdl	bdl	bdl	bdl	bdl	bdl	0.06	7.55
Cr_2O_3	bdl	bdl	0.52	bdl	bdl	0.46	bdl	5.58
FeO	3.32	1.98	6.52	4.03	4.01	5.90	0.06	3.43
NiO	0.24	0.19	0.31	0.16	0.18	0.38	bdl	0.15
Cl	0.02	0.02	0.03	0.02	0.02	0.09	bdl	bdl
H_2O[2]	12.81	12.89	12.62	12.82	12.82	12.65	0.00	4.50
Total wt%	100.92	101.51	100.83	100.55	100.52	101.60	102.74	99.92

bdl = below detection limit

[1] Number of analyses

[2] Determined stoichiometrically